

**MATERIALS DESIGN FROM FIRST PRINCIPLES:
METHODS, MODELS, AND TOOLS**

By

JOHN BONINI

A dissertation submitted to the

School of Graduate Studies

Rutgers, The State University of New Jersey

In partial fulfillment of the requirements

For the degree of

Doctor of Philosophy

Graduate Program in Physics and Astronomy

Written under the direction of

Karin Rabe

And approved by

New Brunswick, New Jersey

October, 2020

ABSTRACT OF THE DISSERTATION

Materials design from first principles: Methods, Models, and Tools

By JOHN BONINI

Dissertation Director:

Karin Rabe

This thesis consists of the development and application of computational methods, models, and tools for investigating and designing functional materials. We begin with an overview of density functional theory, ferroelectricity, the modern theory of polarization, and the present state of the field of first principles materials design. After this review a new first principles method is introduced for computing changes in polarization, referred to as Berry flux diagonalization. This method eliminates the requirement of previous approaches to construct a switching path between oppositely polarized states, enabling for more robust automation, and significantly lower computational cost. Calculations on common ferroelectrics are presented along with comparison to previous approaches. Subsequently, a model for predicting superlattice properties from data computed only for the bulk constituents is presented and expanded to predict dielectric and piezoelectric responses. Several example systems are investigated both with the model and with full superlattice first principles calculations. One such system, $\text{PbTiO}_3/\text{BaTiO}_3$, exhibits an enhanced dielectric response at certain layer ratios. The model can be used to efficiently discover superlattice combinations which give rise to such enhancements, as well to understand the physics which leads to those enhancement.

Finally, a new set of tools for integrating group theoretical methods with first principles calculations and materials databases is introduced. An example application is given where all perovskite structures in the materials project database are identified and classified by the symmetry adapted distortion modes that relate them to the ideal cubic structure. This grouping of structures can be used to identify competing low energy structures of a given material which may be stabilized under certain conditions.

Acknowledgments

This thesis would not have been possible without the guidance, support, and friendship of numerous individuals. I am incredibly grateful to have had a fantastic advisor in Karin Rabe. She introduced me to first principles computational methods as a tool to understand and discover new materials and for that I am eternally grateful. Karin has been incredibly patient with allowing me to approach problems in my own way while still offering invaluable insights. The opportunities Karin has provided me with as well as her personal, professional, and scientific mentorship will continue to influence me throughout not just my career, but my entire life.

The Rutgers condensed matter physics department is an incredible environment for conducting science and I am thankful for the interactions I've had with many current and former members. The joint group meetings with the groups of both Karin Rabe and David Vanderbilt have been very important to my development as a researcher. David has helped me understand his work on the modern theory of polarization which has been vital to much of my research. Premi Chandra has been wonderful to work with on modeling superlattice systems and defects. Don Hammon's presence group meetings and expertise on pseudopotentials and familiarity with the Abinit code base have been invaluable.

I've had the opportunity to work with a number of post doctoral researchers at Rutgers who have been incredibly helpful in both practical aspects of conducting my research as well as facilitating my professional development. In particular Sebastian Reyes-Lilo, Joseph Bennett, and Cyrus Dreyer deserve special thanks. Other current and former group members have been helpful and great to work with including Bartomeu Monserrat, Se Young Park, Yubo Qi, Jinwoong Kim, Subhasish Mandal, Sobhit Singh, Konrad Genser, Heung Sik Kim, Michele Kotiuga, Nicodemos Varnava, Yuanjun Zhou, Meng Ye.

I've made a number of other friends in the Rutgers physics department who have made my time here much more enjoyable including Colin Rylands, David Walter, Sean Burcher, Raghav Kunnawalkam-Elayavalli, John Wu, Kartheik Iyer, Jesse Rivera, Jesus Rives, Wil-low Kion-Crosby, Ghanashyam Khanal, Ian Laflotte, and Caitlin Carpenter.

I'd also like to thank Shirley Hinds and Denise Rafferty for there incredible patience and assistance in navigating the bureaucracy of the university.

I have been lucky enough to have a number of friends and family support me through my academic career. Thank you to my friends Scott, Zack, Waco, Mike, Jeremy, Lavi, Steph, Tim, and the rest of you. I also want to thank my aunt Ann, my uncle Eric, and my cousin Eric who is like a brother to me. Special thanks to my girlfriend Hershi who has been with me while this is being written as we practice social distancing during the COVID-19 pandemic. Finally, I want to thank my parents John and Mary for their support, encouragement, and love.

Dedication

For Mollie

Table of Contents

Abstract	ii
Acknowledgments	iv
Dedication	vi
List of Tables	x
List of Figures	xi
1. Introduction	1
2. Background	5
2.1. Density functional theory	5
2.1.1. DFT Foundations and Kohn-Sham equations	5
2.1.2. Practical implementations	7
2.2. Ferroelectricity	9
2.3. The modern theory of polarization	10
2.4. First principles materials design	14
2.4.1. High throughput calculations and databases	15
2.4.2. Crystal structure and group theory methods	18
3. Methods: Berry Flux Diagonalization	21
3.1. Introduction	21
3.2. Formalism	22
3.2.1. Background and notation	22

3.2.2.	Gauge class	24
3.2.3.	Discrete k space	26
3.2.4.	Gauge invariant formulation	27
3.2.5.	Berry flux diagonalization	28
3.2.6.	Ionic contribution and alignment	29
3.3.	Methods	31
3.4.	Results	32
3.5.	Discussion	35
3.5.1.	Comparison to fictitious path approach	35
3.5.2.	Relation to Wannier functions	37
3.5.3.	Conditions for applicability	37
3.6.	Conclusion	38
4.	Models: Bulk layer model for superlattices	39
4.1.	Introduction	39
4.2.	Methods	41
4.2.1.	Bulk-Layer Model	41
4.2.2.	First Principles Calculations	42
4.3.	Results	43
4.3.1.	Electric-Elastic Constitutive Relations	43
4.3.2.	Superlattice Properties	44
4.4.	Discussion	45
4.4.1.	Analysis of Model Results	45
4.4.2.	Comparison With First Principles Results	48
4.5.	Supplementary Material	49
4.5.1.	Determination of electric-elastic constitutive relations	49
4.5.2.	First-principles linear-response calculations with epitaxial constraints	51

4.5.3. Comparison of linear response and model (finite difference) for bulk constituents	52
4.5.4. Three Component Superlattices	53
4.6. Conclusions	54
5. Tools: Integration of first principles calculations, databases, and group theoretical methods	60
5.0.1. Introduction	60
5.0.2. Pysotropy functionality	61
5.0.3. Application: Identifying most common perovskite structures in the Materials Project database	64
6. Conclusions and outlook	71
References	74

List of Tables

4.1. Computed structural parameters and polarization (P) of each epitaxially constrained constituent material.	53
4.2. Comparison of finite field (FF) and linear response (LR) results for the dielectric permittivity (ϵ_{33}) and piezoelectric responses ($d_{33} = \frac{1}{c} \frac{dc}{dE}$ and $g_{33} = \frac{1}{c} \frac{dc}{dD}$) of each epitaxially constrained material.	54
5.1. High symmetry cubic perovskite structure.	62
5.2. A lower symmetry perovskite structure which can be expressed as a distortion of the structure in table 5.1	62
5.3. Distortion mode definitions and amplitudes that related the structures in tables 5.1 and 5.2	64
5.4. Possible order parameter directions of the $K6$ irrep distortion mode and the resulting lower symmetry space group for graphene.	65
5.5. Components of the general $K6$ distortion mode which with all components active mixes distortions from multiple K points.	65
5.6. Perovskite structure prototypes with ICSD entries in materials project and their associated spacegroup and symmetry adapted distortion modes from the cubic ($Pm\bar{3}m$) structure sorted by number of entries present in the database. The Irrep symbol is given along with a symbol specifying the order parameter direction. The symbols for the order parameter directions were chosen by Stokes and Hatch, and are a way of classifying equivalent directions. The final row indicates the 33 structures for which only one example of that structure type is present.	69

List of Figures

2.1.	An experimental setup to measure polarization in a ferroelectric is shown in (a) with the resulting hysteresis loop in (b). The region in (b) where the sample moves from the origin to the upper right represents initially random domains being aligned by the field. Figure from [1].	11
2.2.	Materials databases timeline and geographic locations, from [2].	17
3.1.	Sketch of the joint (k, λ) space for computing a change in polarization between λ_A and λ_B . Blue circles represent points where Bloch wavefunctions have been computed. The light grey box represents the surface S that is integrated over in Eq. (3.2). Dotted green lines represent the plaquets i and the solid green lines represent the path on which the parallel transport procedure is performed around the green plaquet it encloses to obtain its contribution to $P^B - P^A$	30
3.2.	Histogram of Wilson loop eigenvalues (ϕ_n^p from Eq. (3.27)) for the plaquets highlighted in the insets following the form of Fig. 3.1. In each of the two middle plots, the two highlighted plaquets have identical contributions due to time reversal symmetry. Values for pure PbTiO_3 are shown on the right. The occurrences of values for the primitive and supercell systems differ only by a factor of 4 as indicated by the two axis scales at the top and bottom of the figure. Values for $\text{PbZr}_{0.25}\text{Ti}_{0.75}\text{O}_3$ are shown at left.	33
3.3.	Singular values throughout the Brillouin zone for PbTiO_3 , sampled on a $12 \times 12 \times 12$ Γ centered k mesh.	34

3.4.	Evolution of formal polarization of PbTiO_3 along a linearly interpolated switching path for the primitive cell (left) and a $2 \times 2 \times 1$ supercell (right). Ticks and horizontal lines mark the polarization quantum. The blue arrow indicates the change in polarization, which with the Berry flux diagonalization method only requires calculations in the initial state and symmetry-related final state.	36
4.1.	Computed electric-elastic constitutive relations for SrTiO_3 , BaTiO_3 , and PbTiO_3 . Filled circles show the calculated values and the solid curves are spline fits. The definite parity of each function is used to obtain the results for negative D . The insets zoom in on the slight polar instability computed for SrTiO_3 . The bottom figure shows the derivatives of the spline fits shown in the E plot with respect to D	56
4.2.	Spontaneous polarization, tetragonality (c/a), dielectric response κ_{33} and piezoelectric response d_{33} for (a) $\text{PbTiO}_3/\text{BaTiO}_3$, (b) $\text{BaTiO}_3/\text{SrTiO}_3$ and (c) $\text{PbTiO}_3/\text{SrTiO}_3$, plotted as functions of the layer fraction x of the lower polarization constituent. The bulk-layer model results are shown by a solid line and the first-principles results for individual superlattices are shown as circles filled by colors corresponding to the total superlattice period. The insets in the panels for κ_{33} and d_{33} of $\text{PbTiO}_3/\text{BaTiO}_3$ show the first-principles values for $n:n$ superlattices ($x = 0.5$) plotted against $(1 - 1/N)$, where N is the superlattice period in layers of bulk unit cells, with a linear fit to the $N > 2$ values showing accurate convergence to the model value (indicated by the horizontal line). The differing scales of the vertical axes in each figure are chosen to accommodate the differing ranges over which properties vary between systems. The imperfect agreement between the end points and the model is discussed in the supplemental material.	57

4.3. Model and first principles results for $g_{33} = \frac{1}{c} \frac{dc}{dD}$ for (a) PTO/BTO, (b) BTO/STO, and (c) PTO/STO as functions of layer fraction x of the lower polarization constituent. The bulk-layer model results are shown by a solid line and the first-principles results for individual superlattices are shown as circles filled by colors corresponding to the total superlattice period.	58
4.4. Results for three component superlattices	59
5.1. Supercell of the cubic perovskite structure given in table 5.1. Arrows indicate the displacements which form the distortion mode of Irrep X1+ along the $0, 0, a$ direction leading to the structure in table 5.2.	63
5.2. Components of the K6 graphene distortion corresponding to those in table 5.5. The K6 order parameter can be viewed as a four dimensional vector which describes the distortion as a linear combination of the distortions shown. Directions of this vector and the symmetries that result are given in table 5.4.	66
5.3. Narrowing down structures in materials project from those which satisfy the ABC_3 stoichiometry to those which have been seen experimentally and are small distortions of the cubic perovskite structure.	68

Chapter 1

Introduction

Functional materials have properties that can be controlled by external electric, magnetic, optical, chemical, mechanical, or other stimuli. In this thesis, particularly chapters 3 and 4, focus is given to control via external electric fields, which occurs primarily through coupling to the electric polarization. All insulators exhibit a coupling between polarization and electric field known as the dielectric effect. In piezoelectric materials there is an additional coupling between the polarization and the strain so that applied strains change the polarization, and applied electric fields change the strain. Some systems have a polarization even in the absence of any applied electric field, this is referred to as a “spontaneous polarization”. Such materials will have several equivalent states where the spontaneous polarization is oriented in different directions. If an applied electric field can induce a reversible switching between these states the material is considered to be ferroelectric.

Not only do these functional properties involve fascinating fundamental physics, they are also incredibly useful for device applications. Materials with large dielectric constants are used to make efficient capacitors for use in transistors, energy storage devices, and more. Microphones and other sensors use piezoelectrics to convert acoustic vibrations to an electrical signals and piezoelectric stepper motors can operate with nanometer scale precision. The switchability of ferroelectrics allows for applications in memory devices, and the nonlinear response to electric fields of ferroelectrics can be used to produce tunable capacitors.

The ability to understand, tune, and discover functional materials is of great interest both for the novel physics to be discovered as well as for technological applications. Approaching this problem from first principles, through quantum mechanical simulations of

the Schrödinger equation for nuclei and electrons, facilitates this process of understanding, optimization, and discovery. In simulations the microscopic processes that influence macroscopic properties can be observed directly. Certain interactions and degrees of freedom can be artificially suppressed to discover the relevant physics for particular phenomenon. Parameters that would be difficult to control experimentally can be explored with ease to find values which optimize a given property. New materials can have their properties investigated prior to engaging in challenging or expensive synthesis techniques. Materials design from first principles has had great success already and further developments in theoretical methods, models, and tools are vital to expand and accelerate this process.

In this dissertation we further develop these methods, models, and tools then apply them to a number of real materials. First principles methods can be improved with techniques which are more computationally efficient, easier to automate, and explicit in the applicability of their approximations. Models can be further developed to better understand more material properties allowing for engineering of new materials where these properties are enhanced. The software tools which enable researchers to utilize these methods and models can be made easier to automate and better integrated with the rest of the materials science software ecosystem.

Chapter 2 reviews essential background material. First, the core methodology of our first principles calculations, density functional theory, is introduced. Next, ferroelectricity and the modern theory of polarization are reviewed giving more details on the nature of electric polarization, how it is measured, and how it is computed. Finally, a brief overview is given of the current state of “first principles materials design” including information on high throughput calculations, the databases they populate, and symmetry based methods for analyzing crystal structure data.

In chapter 3 a new more efficient method of computing changes in polarization is developed. Computation of polarization in crystal systems has been enabled by the modern theory of polarization, where it is expressed in terms of a change in Berry phase as the material switches. It is straightforward to compute this change of phase, but only modulo 2π , requiring a branch choice from among a lattice of values separated by 2π . The measured

switching polarization depends on the actual path along which the material switches. This generally involves nucleation and growth of domains and is therefore quite complex. We present an approach for predicting the experimentally measured polarization change that requires only knowledge of the initial and final states, based on the empirically derived principle that for most ferroelectrics the observed polarization change is the same as for a path involving minimal evolution of the state. The result of this minimal evolution of the electronic wavefunction is found by separating the change in phase between two multi-electron wavefunctions into as many gauge-invariant smaller phase changes as possible and then taking each of these to be on the smallest magnitude branch choice. We show that for typical ferroelectrics this technique allows the switching polarization to be computed without any need for intermediate sampling between oppositely polarized states. This work is has been submitted for publication and is currently available on arXiv [3].

In chapter 4 a model for computing superlattice properties using only information computed for the constituent bulk materials is presented, further developed, and applied to several systems. In the first-principles bulk-layer model the superlattice structure and polarization are determined by first-principles computation of the bulk responses of the constituents to the electrical and mechanical boundary conditions in an insulating superlattice. In 4 the model is extended to predict functional properties, specifically dielectric permittivity and piezoelectric response. A detailed comparison between the bulk-layer model and full first-principles calculations for three sets of perovskite oxide superlattices, $\text{PbTiO}_3/\text{BaTiO}_3$, $\text{BaTiO}_3/\text{SrTiO}_3$ and $\text{PbTiO}_3/\text{SrTiO}_3$, is presented. The bulk-layer model is shown to give an excellent first approximation to these important functional properties, and to allow for the identification and investigation of additional physics, including interface reconstruction and finite size effects. Technical issues in the generation of the necessary data for constituent compounds are addressed. These results form the foundation for a powerful data-driven method to facilitate discovery and design of superlattice systems with enhanced and tunable polarization, dielectric permittivity, and piezoelectric response. This work has been published in Physical Review B[4].

In chapter 5 the development and application of the pysotropy library for integrating

group theoretical methods and large databases of materials data is presented. The capabilities of the library are introduced with small scale examples on single materials. The advantage of such tools being interfaced with existing materials libraries and databases through pymatgen is demonstrated by an example on the entire perovskite class of materials.

In chapter 6 we summarize key results and look ahead to new extensions and applications of the discoveries presented in this thesis.

Chapter 2

Background

2.1 Density functional theory

The first principles approach to the study of materials is to solve the many-body Schrödinger equation for the materials of interest. The particles involved for the energy scales of interest are the nuclei and the electrons. Since nuclei are at least three orders of magnitude more massive and thus react to forces on a much larger time scale the electrons can often be treated as if the nuclei are fixed. This is known as the Born-Oppenheimer approximation. Then the many-body Schrödinger equation becomes

$$\left[\sum_i \left(-\frac{\hbar^2}{2m_e} \nabla_{\mathbf{r}_i} + \frac{e^2}{2} \sum_{j \neq i} \frac{1}{|\mathbf{r}_i - \mathbf{r}_j|} - \frac{e^2}{2} \sum_I \frac{Z_I}{|\mathbf{r}_i - \mathbf{R}_I|} \right) \right] \psi(\{\mathbf{r}_i\}) = E\psi(\{\mathbf{r}_i\}) \quad (2.1)$$

where \mathbf{r}_i is the position of electron i and Z_I and \mathbf{R}_I are respectively the charge and position of nuclei i . The computational cost of solving Eq. 2.1 by diagonalization scales exponentially with the number of electrons and becomes practically impossible for all but very small systems. For macroscopic materials another approach is needed.

2.1.1 DFT Foundations and Kohn-Sham equations

Density Functional Theory (DFT) has been an enormously successful approach for computing the ground state energy and electronic structure of materials[5, 6]. The foundation of DFT came from Hohenberg and Kohn in 1964 [7] in the form of two theorems. The first of these theorems states that the total ground state electron density $\rho(\mathbf{r})$ completely and exactly determines all ground state properties of a many electron system. More explicitly Hohenberg and Kohn prove that the external potential (the final term in the Hamiltonian of Eq. 2.1) has a one to one mapping to the charge density $\rho(\mathbf{r})$. Thus for the ground

state of the system the density determines the external potential, which determines the wavefunctions ψ , which contains all information about the electronic state. The second Hohenberg-Kohn theorem proves the existence of an energy functional of the electron density, the minimization of which leads to the exact ground state energy and charge density.

It was not until a year later in 1965 that Kohn and Sham proposed an equation for this functional[8]. With the density of the system given in terms of orthonormal orbitals ψ_i

$$\rho = \sum_i |\psi_i|^2 \quad (2.2)$$

the Kohn-Sham total energy functional is

$$E(\rho) = -\frac{\hbar^2}{2m} \sum_i \langle \psi_i | \nabla^2 | \psi_i \rangle + \frac{e^2}{2} \int \frac{\rho(\mathbf{r})\rho(\mathbf{r}')}{|\mathbf{r} - \mathbf{r}'|} d\mathbf{r}d\mathbf{r}' + \int V_{\text{ext}}\rho(\mathbf{r})d\mathbf{r} + E_{\text{XC}}[\rho(\mathbf{r})] \quad (2.3)$$

where V_{ext} is the external potential due to the nuclei and E_{XC} is the “exchange-correlation” functional to be discussed more at the end of this section.

Minimizing the energy in Eq. 2.3 with respect to the orbitals ψ_i yields the Kohn-Sham equation

$$\left[-\frac{\hbar^2}{2m} \nabla^2 + \int \frac{e^2 n(\mathbf{r}')}{|\mathbf{r} - \mathbf{r}'|} d\mathbf{r}' + V_{\text{ext}}(\mathbf{r}) + \frac{\delta E_{\text{XC}}}{\delta \rho(\mathbf{r})} \right] \psi_i = \epsilon_i \psi_i \quad (2.4)$$

Where the term $\delta E_{\text{XC}}/\delta \rho(\mathbf{r})$, referred to as the “exchange-correlation potential”, is a functional derivative of E_{XC} with respect to $\rho(\mathbf{r})$. With this choice of energy functional and subsequent minimization the many body problem has now been mapped on to a non interacting system of particles in an effective potential which can be solved self consistently. This treatment is exact even for strongly correlated systems. The approximation comes in the treatment of E_{XC} and its functional derivative.

In order to solve Eqs. 2.4 approximations to the exchange-correlation potential are needed. The earliest and simplest of such approximations, which was proposed by Kohn and Sham, is the “local density approximation” (LDA). With LDA one approximates E_{XC} as

$$E_{\text{XC}} = \int \epsilon_{\text{XC}}(\rho(\mathbf{r}))d\mathbf{r} \quad (2.5)$$

where $\epsilon_{\text{XC}}(\rho(\mathbf{r}))$ is the exchange-correlation energy per unit volume of a homogeneous electron gas of density $\rho(\mathbf{r})$. For such a simple approximation it has been remarkably successful. There have been numerous attempts to improve the exchange correlation functional by including a dependence on more than just the local density. The generalized gradient approximation (GGA) includes dependence on the gradient of the density in to the functional, meta-GGA approaches include dependence on the kinetic energy density, and other approaches add additional terms such as Van der Waals or Hartree-Fock style exact exchange corrections. Depending on the physics present in a particular system some functionals perform better than others, but a general functional with significantly improved accuracy over LDA has yet to be found.

The ability to find the ground state and its energy for a given configuration of ions enables the computation of many other properties. The energy of the system can be minimized with respect to these atomic positions (aka relaxation) to find the ground state structure[9]. The electric polarization of a given state can be computed as described in Sec. 2.3 and Ch. 3. Derivatives of the total energy and polarization with respect to various perturbations of the external potential can be used to compute other properties such as forces on atoms, phonon modes and frequencies, dielectric and piezoelectric susceptibility, and more. Such derivatives can be computed either by finite differences or using perturbation theory [10]. The latter often being more computationally efficient, but more complex to implement.

2.1.2 Practical implementations

In principle 2.4 can be solved numerically in any complete basis. The optimal choice typically depends on the sort of system being investigated. When studying materials we are typically interested in systems which form a crystal lattice where some primitive unit cell is repeated on the order of 10^{23} times. In this situation the impact of the system boundary on the material properties is often negligible and we can model the material as if it were an infinite crystal by using periodic boundary conditions. Then within the DFT framework we are typically interested in solving Eq. 2.4 where $V_{\text{ext}}(\mathbf{r})$ is periodic in three dimensions. Since this Hamiltonian commutes with the lattice vector translation operators the eigenfunctions

which solve the equation are Bloch waves of the form

$$\psi_{n,\mathbf{k}}(\mathbf{r}) = e^{i\mathbf{k}\cdot\mathbf{r}}u_{n,\mathbf{k}}(\mathbf{r}) \quad (2.6)$$

where $u_{n,\mathbf{k}}$ is a periodic function has the same periodicity in \mathbf{r} as the lattice and \mathbf{k} is a wave vector in reciprocal space. In practical numerical calculations a mesh of k points are chosen and summed to obtain total energies or other properties[11].

Now the Kohn-Sham equation (Eq. 2.4) can be solved independently at each k , but we still need a basis choice for $u_{n,k}$. Since k -space is also periodic with reciprocal lattice vectors \mathbf{G} plane waves are a convenient and common choice and was used in all calculations in this thesis. The periodic part of the wavefunction is expanded as

$$u_{n,\mathbf{k}} = \sum_G c_{n,\mathbf{k}}(\mathbf{G})e^{i\mathbf{G}\cdot\mathbf{r}} \quad (2.7)$$

then

$$\psi_{n,\mathbf{k}} = \sum_G c_{n,\mathbf{k}}(\mathbf{G})e^{i(\mathbf{G}+\mathbf{k})\cdot\mathbf{r}}. \quad (2.8)$$

In principle an infinite number of plane waves \mathbf{G} are needed, but in practice one truncates the sequence by specifying an energy cutoff E_{cut} and only including plane waves where $\frac{\hbar^2}{2m}|\mathbf{k} + \mathbf{G}|^2 < E_{\text{cut}}$.

The core orbitals near nuclei require a very large value of E_{cut} to represent with plane waves, leading to enormous computational cost. There are several ways to deal with these core states, a common choice, which is used throughout this thesis is the pseudopotential method. In this approach the nuclei and core electrons are replaced with an effective potential experienced by the valence electrons. This potential is constructed in a manner that leaves the valence electron wavefunctions outside the core region identical to what they would be in the all electron case. This dramatically reduces the required value of E_{cut} . Since the core electrons are typically independent of the atomic environment and most physical properties are determined by the valence states this is usually a safe approximation. Norm conserving pseudopotentials are a common choice for their simplicity, they keep the norm of the pseudo-wavefunction the same as the all electron wavefunction within the cutoff radius[12]. Other approaches, such as ultrasoft[13] and PAW[14], are more complex in

implementation, but reduce further the required value of E_{cut} saving on computational cost.

2.2 Ferroelectricity

A material is said to be ferroelectric if it has a multiple electric polarization states in the absence of an electric field which can be switched to other orientations by an external electric field [15]. The majority of known ferroelectrics can be described as having a small distortion from some higher symmetry (often nonpolar) non-ferroelectric reference structure. For many ferroelectrics this reference structure actually exists as a higher temperature phase, though for some systems such a hypothetical phase transition occurs at a temperature above the materials melting point. For most known ferroelectrics the polarization decreases with increasing temperature until it vanishes at some critical temperature. This may be due to an order-disorder transition where local dipoles align with decreasing temperature, or a displacive transition where with decreasing temperature the atoms under go small displacements from some reference phase to the ferroelectric phase.

The switching behavior for a ferroelectric system with two oppositely oriented polarization states can be characterized by the hysteresis loop shown in Fig.2.1 b. At zero applied field the system (or a majority of it) is oriented in one of the two states. Upon application of a field opposite the initial polarization microscopic polar moments decrease and regions of the system (domains) can reverse direction to align with the applied field. As the magnitude of this field increases more of the system can also orient in this direction (the domains grow) and/or microscopic polar moments can increase until the system saturates and the curve flattens. The field can then decrease in magnitude until it reaches zero potentially reversing or lowering the magnitude of some microscopic moments, but maintaining a majority oriented opposite the original polarization direction. The process can be repeated with another reversal returning the system to its original state. The microscopic physics of the switching dynamics which lead to the hysteresis loop are the energy barrier and polarizability of a local portion of the system to switch as well as the effects of domain wall

formation and motion.

2.3 The modern theory of polarization

Polarization is a key property in describing and characterizing ferroelectrics and how insulators interact with electric fields. How to compute polarization for a system modeled with periodic boundary conditions was not clear (and even the possibility was questioned) until the development of the “modern theory of polarization” in the 1990s by Resta[16, 17], King-Smith, and Vanderbilt[18]. Older definitions of polarization involving integration of charge density are problematic with periodic boundary conditions as a different choice of unit cell can yield different values.

To understand the solution to this problem it is constructive to consider that experimentally polarization is not measured directly. Instead one measures the current that flows when polarization is switched. As shown in Fig. 2.1 the ferroelectric is placed in a Sawyer-Tower circuit where voltage oscillates over time and the current over time is measured. The resulting hysteresis loop has the electric field (from the voltage and sample thickness) on the horizontal axis and the time integrated current on the vertical axis, now labeled P . So what is actually measured is the integrated current as the system switches between oppositely polarized variants. This quantity is not the polarization in any one state, but the change in polarization during switching.

The current density is related to this change in polarization between initial state i to a final state f

$$\Delta \mathbf{P} = \int_i^f \mathbf{J}(t) dt. \quad (2.9)$$

The explicit time dependence above can be avoided by considering a system evolving adiabatically with the evolution parameterized by λ

$$\mathbf{J} = \frac{d\mathbf{P}}{dt} = \frac{d\mathbf{P}}{d\lambda} \frac{d\lambda}{dt}. \quad (2.10)$$

Then the change in polarization becomes

$$\Delta \mathbf{P}_{i \rightarrow f} = \int_i^f \left(\frac{d\mathbf{P}}{d\lambda} \right) d\lambda. \quad (2.11)$$

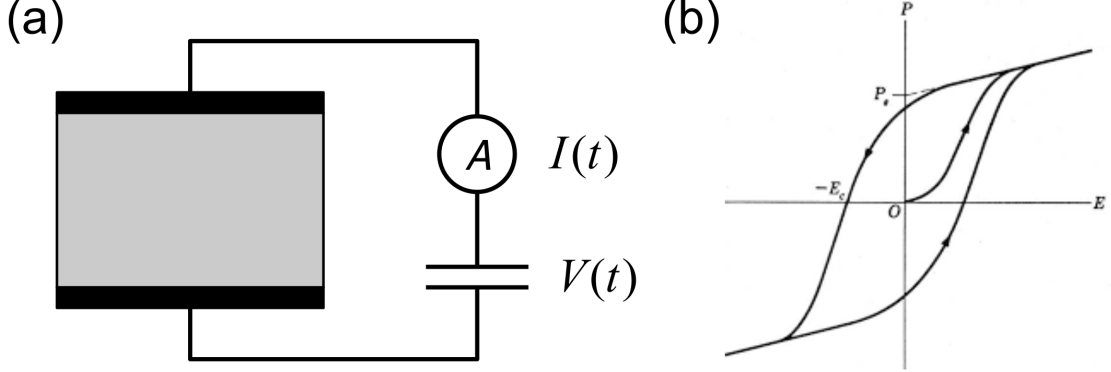


Figure 2.1: An experimental setup to measure polarization in a ferroelectric is shown in (a) with the resulting hysteresis loop in (b). The region in (b) where the sample moves from the origin to the upper right represents initially random domains being aligned by the field. Figure from [1].

Applying perturbation theory techniques (see chapter 4 of [1]) it can be shown that for the electronic contribution to the integrand can be written in terms of the cell periodic part of the Bloch wavefunctions

$$\left(\frac{d\mathbf{P}}{d\lambda}\right)_{\text{el}} = \frac{e}{(2\pi)^3} \sum_n^{\text{occ}} \int_{BZ} 2\text{Im} \langle \partial_\lambda u_n(\mathbf{k}, \lambda) | \partial_{\mathbf{k}} u_n(\mathbf{k}, \lambda) \rangle d^3k. \quad (2.12)$$

By combining Eq. 2.11 and Eq. 2.12 we can obtain an expression for the electronic contribution to the change in polarization along the path parameterized by λ . For simplicity and consistency with Ch. 3 equations here are written for the one dimensional case

$$\Delta P_{\lambda_i \rightarrow \lambda_f} = \frac{-e}{2\pi} \int \int_S \Omega(k, \lambda) d\lambda dk \quad (2.13)$$

where $\Omega(k, \lambda)$ is the Berry curvature given by

$$\Omega(k, \lambda) = \sum_n -2\text{Im} \langle \partial_\lambda u_n(k, \lambda) | \partial_k u_n(k, \lambda) \rangle. \quad (2.14)$$

As shown in Sec. 3.2.1 as well as [1] and [18] this can be expressed in terms of only the end points if the notion of “formal polarization” is introduced.

$$\Delta P = P_{\text{formal}}(\lambda_f) - P_{\text{formal}}(\lambda_i) \quad (2.15)$$

where P_{formal} is the Berry phase across the Brillouin zone

$$P_{\text{formal}}(\lambda) = \frac{-e}{2\pi} \int_{-\pi/a}^{\pi/a} \sum_n i \langle u_n(k, \lambda) | \partial_k u_n(k, \lambda) \rangle dk \quad (2.16)$$

It may seem as though the dependence on the path λ has been eliminated, however the difference to be taken in Eq. 2.15 is more subtle than it initially appears. Since the BZ integral in Eq. 2.16 is a Berry phase, and being a phase is only well-defined modulo 2π , the formal polarization is also only defined modulo a “polarization quantum” P_q . How the difference between these multivalued quantities is to be evaluated is the subject of Ch. 3 where a new method is developed and compared to previous approaches.

The equivalence of Eq. 2.15 and Eq. 2.13 is critically dependent on the gauge choice for the $(|u_n(k, \lambda)\rangle)$. A (k, λ) -dependent unitary rotation among the occupied states $|u_n(k, \lambda)\rangle$ can change ϕ_{λ_A} and ϕ_{λ_B} , and their difference, by multiples of 2π [18, 1] reflecting the multivalued nature of P_{formal} on its own.

The physical interpretation of these quantities which are gauge invariant modulo some factor is that the ambiguity is an expression of what can be known given limited information. When the precise surface termination of the material is not known the dipole moment divided by the volume of a material can not be known. However, from knowledge of the bulk wavefunctions a discrete set of possible values can be computed one of which will be that dipole moment per volume. This discrete set of values is the formal polarization. The measured change in polarization during switching doesn't depend on this surface termination, but it does in general depend on the switching path. So when one does not know the precise path by which the system switches the change in polarization can not be known. However, with the knowledge of the initial and final formal polarizations a discrete set of possible changes can be computed. These are the possible ways of connecting the formal polarization branches between initial and final states. One of these values will correspond to the actual change in polarization.

To avoid confusion we should distinguish between three types of gauge related quantities. There are quantities which are “fully gauge dependent”, where a change in gauge can continuously alter the value of this quantity. The phase difference between wavefunctions at

two arbitrary k -points (a Berry connection or Berry potential) is an example of such a “fully gauge dependent” quantity. Then there are quantities which are gauge invariant modulo some factor or “lattice valued gauge invariant” where a change in gauge can only change the quantity by an integer number of some factor. The integrated change in wavefunction phase around some closed loop (a Berry phase) is an example of a lattice valued gauge invariant quantity which is gauge invariant modulo 2π . Finally, there are quantities which are “fully gauge invariant”, where a change in gauge has no effect on the value at all. The change in Berry phase along some *continuous* path (a Berry flux, or integral of Berry curvature) is an example of such a “fully gauge invariant” quantity.

It is often possible to compute a lattice valued gauge invariant quantity where one of the values corresponds to a fully gauge invariant quantity, but the fully gauge invariant formulation requires more information. The expression for the change in polarization in Eq. 2.13 is fully gauge invariant, however it requires the wavefunctions for all k, λ . On the other hand the expression for ΔP from Eq. 2.16 and Eq. 2.15 is lattice valued gauge invariant and only requires wavefunctions on the boundary of region S . The gauges for which the lattice valued result (Eq. 2.16 and Eq. 2.15) give the precise result one would obtain from the fully gauge invariant formulation (Eq. 2.13) are those where the wavefunctions are smooth (continuous and differentiable) throughout the interior of S . Constructing such a gauge still requires knowledge of the interior of S . In numerical calculations where we wish to work with the ground state wavefunctions and the space is sampled on a mesh it may be impossible to compute the quantity in the fully gauge invariant formulation. Then some other approach is needed to obtain the desired fully gauge invariant quantity.

Previous methods for making the branch choice for a polarization change rely on implicit construction of a smooth gauge by dense sampling in λ as well as k . The typical approach is to specify a path, almost always a fictitious one, but notably one that involves something close to minimal evolution of the ionic positions. Then one samples densely enough along this path until it can be assumed that the change in formal polarization between neighboring points along the path is the smallest in magnitude of allowed values. The total change is then the sum of these smaller changes. These smaller changes are still

computed from a formulation that in principle only gives values which are lattice valued gauge invariant where the lattice spacing is the polarization quantum. However, if the two states are close enough the smallest of allowed values can be assumed to correspond to what would be obtained with a smooth gauge. A common misconception is that to compute the change in polarization as a ferroelectric switches between oppositely polarized states this fictitious path must pass through a centrosymmetric structure. If the chosen path does pass through such a structure one can conveniently only compute the change in formal polarization along half the path, since the path itself will then be symmetric. However, there is nothing incorrect about computing the change along a path between up and down without passing through a centrosymmetric structure. It is the integrated current between oppositely polarized states we are interested in at the end of the day. The change in polarization from a centrosymmetric to polar structure may be relevant as a thermodynamic quantity describing a phase transition from that high symmetry structure, but this value does not necessarily correspond to the integrated current during switching.

The polarization along path procedure for making a branch choice assumes minimal evolution of the ionic positions between states. It also assumes minimal evolution of the formal polarization between steps along the path. These assumptions have proven quite successful in predicting experimentally measured changes in polarization. In chapter 3 we present a related assumption and methodology that enables polarization changes to be computed without the need to construct and sample along a path.

2.4 First principles materials design

Density functional theory and other first principles methods are powerful tools where from the elements present the properties of that real or as-yet hypothetical material can be computed[19]. Materials design is about the inverse of this problem, where a set of desired properties are taken as input and materials which exhibit these properties are identified[20]. This is a challenging problem, but one where solutions can lead to the discovery of materials with desirable properties for practical applications as well as those which exhibit new

physics.

There are various approaches to first principles materials design. For example, a given material with properties near the desired regime can be tuned through chemical substitution, strain, or other parameters. A successful example of such an approach was the magnetoelectric EuTiO_3 , where first principles found the system becomes ferroelectric with small amounts of strain[21]. On the other hand high throughput calculations, where the properties of hundreds up to tens of thousands of candidate materials are computed, can apply a combinatorial approach to the problem. This sort of a approach was successfully applied to predict a new high quality phosphor, $\text{Sr}_2\text{LiAlO}_4$ [22]. The high throughput and parameter tuning approaches can complement one another. The data on a large variety of materials from high throughput calculations can be used to identify starting systems which can be tuned to the desired regime. Furthermore, the high throughput data could be used to find trends across many systems to suggest which parameters are correlated with which properties. The complementary nature of these approaches can be enhanced by integrating them with modeling. Models can be inspired by trends in high throughput data or even parameterized by such data. The model can then be utilized to understand and identify how different parameters impact various properties so that nearby systems can be tuned effectively. Models can also be used in identifying candidate systems, for example if the model requires particular symmetries to achieve the desired properties this can narrow down which materials are enumerated in a high throughput computation and these results can help identify promising systems for further tuning[23].

2.4.1 High throughput calculations and databases

The idea of combinatorial evaluation of material properties is over a hundred years old going back to Edison. However, it is in recent times that theoretical methods and computational resources have become powerful enough to make the virtual analog of this process viable. To obtain experimental results for a given material it is often the case that the synthesis step is incredibly time consuming, difficult, and expensive. Synthesis for a “virtual experiment” is an essentially trivial process. Furthermore, calculations can be automated such that a single

researcher can characterize thousands of materials. Calculations can also be more easily performed in such a way that the resulting dataset is uniform in structure, reproducible, and automatically transferred to a database for efficient subsequent analysis. Indeed, one proposed definition of high throughput materials research is that the throughput of data is too large to be produced or analyzed by direct intervention and must be automated [24].

The large scale automation of first principles calculations is a nontrivial task and a number of frameworks and tools have been developed to facilitate the process. Pymatgen is a python library for materials analysis featuring classes for representing and manipulating the basic objects of interest such as elements, sites, molecules, crystal structures, and electronic structures[25]. Pymatgen can automate the creation of input files for several first principles codes, and is also used as a library for other tools such as abipy and aiida. The pymatgen developers have released tools to manage other steps in the calculation process such as Fireworks to manage HPC calculation jobs and Custodian for correcting errors in these jobs on the fly. Abipy is a python library for analyzing the results and automating the calculations of the first principles code Abinit. Aiida is an automated interactive infrastructure and database for computational science which tightly couples calculation automation, HPC job management, and data storage with a focus on data provenance for full reproducibility[26, 27, 28]. The AFLOW project also has its own set of tools used to automate calculations and populate its database[29].

The quantity of data generated by these automated systems is more than a single researcher can analyze manually so must be stored in a database where data can be analyzed by automated means and queried by many researchers. Many databases of both experimental and theoretical properties have been constructed in the last few decades. The International Crystal Structure Database (ICSD) is one of the older databases and contains crystal structures from experimental measurements. The Materials Project database contains computed properties such as band structures, elastic tensors, and piezoelectric tensors on hundreds of thousands of inorganic compounds, molecules, and nanoporous materials. The AFLOW database contains calculated properties on over two million inorganic crystal structures. The Joint Automated Repository for Various Integrated Simulations (JARVIS)

contains data on numerous materials and is notable for using tighter convergence criteria, storing full wavefunctions for later analysis, as well as containing DMFT and GW calculations in addition to DFT. See Fig. 2.2 for a more complete list of databases.

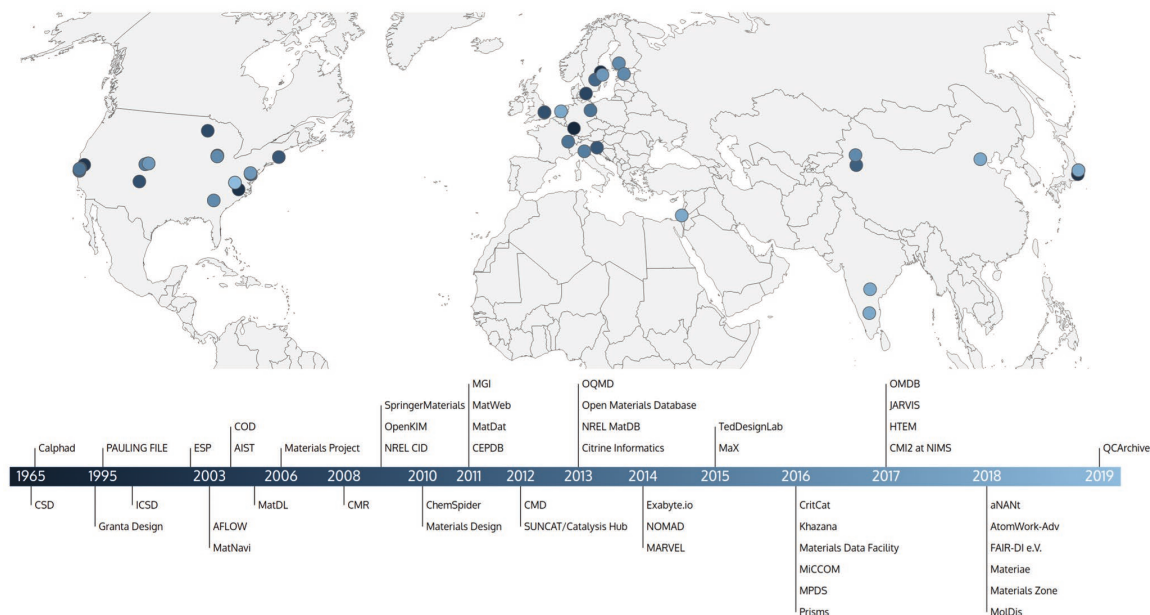


Figure 2.2: Materials databases timeline and geographic locations, from [2].

Though there are many efforts to compute and store data for materials design a number of challenges in the field remain. Some of these challenges are fundamental physics problems such as the treatment of systems with many atoms or strong correlations in a computationally tractable manner. On the other hand there are more sociological challenges such as standardization of materials data formats and creating incentives to share such data [2]. There are a number of quantities that current methods can handle well, but are difficult to automate in their standard implementation[30] such as Wannier functions and changes in polarization. The discovery of descriptors which relate computed microscopic quantities to macroscopic material properties is another area of ongoing research[24]. New ways to utilize all of this data such as machine learning approaches or semi-empirical approaches to difficult problems such as structure determination are also of great interest.

2.4.2 Crystal structure and group theory methods

Symmetry is the most important unifying concept in physics. The relevant symmetry groups when studying materials are the 230 space groups which are the possible symmetry groups for crystals that tile 3D space. Physical properties such as the allowed components of piezoelectric, dielectric, conductivity, and other tensors are determined by the space group symmetry. With group theory methods one can also see that the space group and site occupations of a given crystal structure determine the normal modes of that system[31]. Each normal mode belongs to a particular irreducible representation (irrep) of the space group, the dimension of which determines the degeneracy of that mode, and how that particular irrep transforms determines whether the mode will be Raman or IR active. For degenerate phonon modes there is some choice in how the mode is constructed as linear combinations of degenerate modes do not change the frequencies. However some combinations do change the symmetry of the system when such a mode is frozen in. It can be useful to choose symmetry adapted modes which lead to greater symmetry.

The normal modes of the crystal system are useful for more than describing the spectrum of lattice vibrations. When a system undergoes a symmetry lowering phase transition some of these modes become frozen in. In this context the modes themselves and their amplitudes form a set of order parameters. In the Landau theory of phase transitions the free energy of the system is expressed as a polynomial with terms made up of products of order parameters and their coefficients. The space group of the high symmetry phase and the irreducible representation of the order parameters determine which terms appear in the free energy and thus which terms are coupled.

The symmetry adapted modes are also useful for describing structures which are closely related to some other high symmetry structure. While the set of modes is a complete basis, it is often the case that only a handful of modes are frozen in so this can be a much more convenient description than a list of atomic coordinates in Cartesian space. For example there are numerous perovskite structures which are closely related to the simple cubic structure through a combination of oxygen octahedra rotations, tilts, or breathing patterns

as well as polar distortions. The description of these modes and their relative amplitudes is often much simpler and easier to comprehend than a list of atom positions.

Symmetry and group theory methods can serve as a vital tool in materials design. For example one may be interested in finding materials with coupling between a certain property with an applied electric field. If one can identify an order parameter related to the property then one can narrow down the set of systems to search to those which allow a coupling between that mode and IR active polar modes. For example, there is strong interest in systems where magnetization direction can be influenced by applied electric fields. One strategy has been to search for systems where a polar distortion couples to some other distortion (typically an octahedra rotation) that controls the Dzyaloshinskii-Moriya exchange interaction thus influencing the magnetization[23]. The symmetry of a system determines whether or not this coupling will exist and can be used to find candidate systems which can then be further investigated to find those where the coupling is strong and/or have the desired switching dynamics[32]. More generally, if one identifies a model where the physics of interest occurs when the model possesses certain symmetries one can then look for real systems within spacegroups that preserve those symmetries.

A handful of resources are available for applying group theory methods to crystal structures. Spglib is an efficient software library, used by pymatgen and other tools, for finding crystal symmetries, the space group, Wyckoff position assignments, primitive structure, and irreducible k-points of a structure[33]. The Bilbao crystallographic server[34, 35] is an online resource containing databases of space group data such as Wyckoff positions and irreps as well as various online utilities for analyzing group-subgroup relations and crystal structures. The ISOTROPY software suite contains another set of online utilities for applying group theoretical methods to analyze crystal structures. The ISOTROPY command line utility is available in an offline form[36].

These resources are incredibly useful, but only spglib is currently well integrated with first principles calculation codes, materials databases, and other tools. Many of the currently available tools are only available through a web interface which makes automated analysis of many materials cumbersome. The integration of materials focused group theoretical tools

with first principles codes and materials databases can lead to new insights and approaches to materials design. This integration and its application are the focus of chapter 5.

Chapter 3

Methods: Berry Flux Diagonalization

3.1 Introduction

Bistable systems with a change in electric polarization on switching between the two states are of central importance in functional material and device design. The most familiar of such systems are ferroelectrics, with two or more symmetry-related polar insulating states[15]. Switching in systems in which the two states are not symmetry related, for example in antiferroelectrics or heterostructures, is also of great interest for novel devices[37, 38].

First principles prediction of the switching polarization in periodic systems is based on the modern theory of polarization, which expresses the polarization change between two states in terms of the change in Berry phase as the system evolves along a specified adiabatic path. [18, 1] Given only the initial and final states, the polarization change is determined modulo the “quantum of polarization” ($e\mathbf{R}/\Omega$), where e is the charge of an electron, \mathbf{R} is a lattice vector, and Ω is the volume of the unit cell. The choice from this set that gives the specific value of the polarization change depends on the actual switching path.

Since the path for a process such as electric field switching of a ferroelectric generally involves nucleation and growth of domains, beyond the scope of current first-principles computation, it might at first seem that first-principles prediction of the switching polarization should not be possible. However, it is an empirical fact that good agreement with experimental observation has been obtained for many ferroelectrics by computing the polarization change along a fictitious minimal path, usually constructed by simple linear interpolation of the atomic positions of the up- and down-polarized states, maintaining their lattice translational symmetries [39]. The polarization change along this fictitious path is then computed by sampling densely enough along the path so that the polarization change for every step

along the path can be chosen (and is chosen) to be small compared to the quantum of polarization. However, this method can be computationally intensive, depending on the sampling density required. Moreover, for some systems, it might be that not all the states on the simple linear interpolation path are insulating, and additional effort is required to find an insulating adiabatic path connecting the up and down states. As a result, this approach has proven to be problematic for automated high-throughput applications.

In this chapter, we present a new method for predicting switching polarization given only the initial and final states. Our approach uses information, computed from the two sets of ground state wavefunctions, that goes beyond that used in a conventional Berry phase calculation. The key idea is to incorporate certain assumptions about the physical path, eliminating the need to construct a fictitious path and perform calculations for intermediate states. We begin by discussing the method for the simplest case of the electronic contribution to the switching polarization for a one-dimensional polar insulator. We then generalize to three-dimensional materials and discuss the ionic contribution to the polarization. Finally, first-principles results are presented for a realistic benchmark system to illustrate the various aspects of the method and to compare with the fictitious path method. The approach presented here is not limited to computation of switching polarization in ferroelectrics, but can be applied to the change in polarization between two symmetry-inequivalent states, for example in antiferroelectrics, heterostructures and pyroelectrics, and in the computation of the nonlinear response of insulators to electric fields.

3.2 Formalism

3.2.1 Background and notation

We start by considering a one-dimensional crystal switching between initial state A and final state B along a specified path parameterized by λ , along which the system remains insulating. According to the modern theory of polarization,[18, 16, 1, 39] the electronic contribution to the change in polarization can be expressed as

$$\Delta P_{A \rightarrow B} = \frac{-e}{2\pi} \Phi \quad (3.1)$$

where Φ is the Berry flux

$$\Phi = \int \int_S \Omega(k, \lambda) d\lambda dk \quad (3.2)$$

obtained by integrating the Berry curvature $\Omega(k, \lambda)$ over the region S with $\lambda_A \leq \lambda \leq \lambda_B$ and $-\pi/a < k \leq \pi/a$ (the first Brillouin zone). Here the Berry curvature

$$\Omega(k, \lambda) = \sum_n -2\text{Im} \langle \partial_\lambda u_n(k, \lambda) | \partial_k u_n(k, \lambda) \rangle \quad (3.3)$$

is written in terms of the cell-periodic parts of the occupied Bloch wavefunctions $|u_n(k, \lambda)\rangle$ and has been traced over the occupied bands n . The $|u_n(k, \lambda)\rangle$ are chosen to be differentiable over the surface S and periodic in k . Application of Stoke's theorem gives

$$\Phi = \oint_C \mathbf{A}(\mathbf{q}) \cdot d\mathbf{q} \quad (3.4)$$

where C is the boundary of the surface S , $\mathbf{q} = (k, \lambda)$, and $\mathbf{A}(\mathbf{q}) = (A_k, A_\lambda)$ is the Berry potential given by

$$A_k = \sum_n i \langle u_n(k, \lambda) | \partial_k u_n(k, \lambda) \rangle , \quad (3.5)$$

$$A_\lambda = \sum_n i \langle u_n(k, \lambda) | \partial_\lambda u_n(k, \lambda) \rangle . \quad (3.6)$$

Since we have chosen a periodic gauge in the k direction, the two portions of the path C running in the λ direction cancel. The two remaining segments take the form

$$\phi_\lambda = \int_{-\pi/a}^{\pi/a} A_k(k, \lambda) dk \quad (3.7)$$

and it follows that

$$\Phi = \phi_{\lambda_B} - \phi_{\lambda_A} . \quad (3.8)$$

The electronic contribution to the change in polarization is then given by Eq. (3.1).

The equivalence of Eq. (3.8) to Eq. (3.2) is critically dependent on the gauge choice for the $(|u_n(k, \lambda)\rangle)$. A (k, λ) -dependent unitary rotation among the occupied states $|u_n(k, \lambda)\rangle$ can change ϕ_{λ_A} and ϕ_{λ_B} , and their difference, by multiples of 2π [39, 18, 1], so that the change in polarization is determined only modulo the quantum of polarization $e\mathbf{R}/\Omega$. As we describe more fully below, previous methods for making the correct branch choice for a

given path rely on implicit construction of a smooth gauge by dense sampling in λ as well as k . Here, we present an alternative approach that makes full use of the information contained in the initial and final states, while eliminating the need for sampling at intermediate values of λ . Moreover, this approach requires a k -space sampling no denser than that required for the computation of the formal polarization.

3.2.2 Gauge class

We first consider the case of a single occupied band in 1D with Bloch states $|u(k)\rangle$. Following Eq. (3.8), the Berry phase around the Brillouin zone at a given λ is given by

$$\phi = \int_{-\pi/a}^{\pi/a} \langle u(k) | i\partial_k u(k) \rangle dk \quad (3.9)$$

The requirement that the gauge be smooth and periodic in k allows transformations of the form $e^{-i\beta(k)} |u(k)\rangle$, where $\beta(k)$ is differentiable and $\beta(k + 2\pi/a) = \beta(k) + 2\pi n$ for some integer n , which changes ϕ by $2\pi n$. For a given physical system, we can test whether two choices of gauge a and b will produce the same value of ϕ by computing

$$\gamma^{ab}(k) = \langle u^a(k) | u^b(k) \rangle . \quad (3.10)$$

Note that $\gamma^{ab}(k)$ has exactly unit norm and is just $e^{-i\beta(k)}$, where $\beta(k)$ describes the gauge change relating a to b . If $\gamma^{ab}(k)$ is smooth and its phase does not wind by a nonzero integer multiple of 2π as k traverses the 1D Brillouin zone, the two gauges will produce the same ϕ , and can be said to belong to the same ‘‘gauge class.’’

Next, we consider two crystals A and B with single occupied bands, each with a smooth gauge, and ask whether their respective gauges belong to the same gauge class in a similar sense. With this motivation, we define, in analogy with Eq. (3.10),

$$\gamma^{AB}(k) = \langle u^A(k) | u^B(k) \rangle \quad (3.11)$$

where $\gamma^{AB}(k)$ will generally not have unit norm. In fact, for this procedure to be meaningful, systems A and B must be sufficiently closely related that the norm of $\gamma^{AB}(k)$ remains nonzero everywhere in the Brillouin zone. If the phase of this $\gamma^{AB}(k)$ does not wind by a nonzero integer multiple of 2π , we consider their gauges to belong to the same gauge class.

We are now in a position to introduce our key idea for the prediction of the switching polarization from system A to B . This is that the wavefunction phases evolve along the physical switching path in a minimal way that preserves the gauge class, so that the switching polarization corresponds to the polarization difference of Eq. (3.1) and Eq. (3.8) with Berry phases ϕ^A and ϕ^B computed with the requirement that the two gauges belong to the same gauge class. Crucially, the branch-choice ambiguity in the individual ϕ^A and ϕ^B is no longer present after the difference is taken.

The generalization to the multiband case is straightforward. We define

$$\gamma^{AB}(k) = \det M^{AB}(k) \quad (3.12)$$

where $M^{AB}(k)$ is the overlap matrix given by

$$M_{mn}^{AB}(k) = \langle u_m^A(k) | u_n^B(k) \rangle \quad (3.13)$$

for occupied band indices m and n . The gauges are said to belong to the same class if the phase winding of $\gamma^{AB}(k)$ is zero.

One way to insure that gauges A and B belong to the same gauge class is to align one to the other. In the single-band case, the gauge of B is aligned to that of A by taking $\chi(k) = \text{Im} \ln \gamma^{AB}(k)$, and then letting

$$|\tilde{u}^B(k)\rangle = e^{-i\chi(k)} |u^B(k)\rangle. \quad (3.14)$$

As a result, the new $\tilde{\gamma}^{AB}(k)$ is real and positive, so that there is clearly no winding. Similarly, the multiband gauge alignment can be accomplished by carrying out the singular value decomposition of M^{AB} in Eq. (3.12) as $M^{AB} = V^\dagger \Sigma W$, where V and W are unitary and Σ is positive real diagonal. Then the multiband analog of $e^{i\chi}$ is $U = V^\dagger W$, and the gauge of B is aligned to that of A by the transformation

$$|\tilde{u}_n^B\rangle = \sum_m (U^\dagger)_{mn} |u_m^B\rangle. \quad (3.15)$$

The new overlap matrix is then $\tilde{M}^{AB} = V^\dagger \Sigma V$, whose determinant $\tilde{\gamma}^{AB}$ in Eq. (3.12) is clearly real and positive, thus eliminating the relative winding of gauge B with respect to A .

3.2.3 Discrete k space

In any numerical calculation, functions of k must be sampled on a discrete mesh in k . In this case, we can again align the gauge of B to that of A using Eq. (3.14) or Eq. (3.15), and compute the polarization difference via Eq. (3.8). However, in the discrete case there is a new potential source of ambiguity coming from the need to enforce smoothness with respect to k . After discretization Eq. (3.7) becomes

$$\phi_\lambda = \text{Im} \ln \det \prod_i M^\lambda(k_i, k_{i+1}) \quad (3.16)$$

where M is the overlap matrix

$$M_{mn}^\lambda(k_i, k_{i+1}) = \langle u_m^\lambda(k_i) | u_n^\lambda(k_{i+1}) \rangle . \quad (3.17)$$

This ϕ_λ is gauge invariant, but only up to an integer multiple of 2π . This is reflected by the $\text{Im} \ln$ operation in Eq. (3.16), which will only result in a phase in the interval $-\pi < \phi_\lambda < \pi$. If one is interested in this phase on its own (i.e., for computing formal polarization) this makes perfect sense, since it is truly a lattice valued quantity. However, our present goal is to compute the difference in phase between two systems with the requirement that both systems are in the same gauge class. For this purpose it is useful to rewrite Eq. (3.16) in a form where values outside this interval are possible (with the branch being determined by the gauge). To this end we rewrite Eq. (3.16) as

$$\phi_\lambda = \sum_i \mathcal{A}_i(\lambda) \quad (3.18)$$

where

$$\mathcal{A}_i(\lambda) = \text{Im} \ln \det M_\lambda(k_i, k_{i+1}) \quad (3.19)$$

is a discrete analog of the Berry connection A_k . We choose a sufficiently fine k mesh and a sufficiently smooth gauge so that each \mathcal{A}_i is much less than π in magnitude; then ϕ^A can be unambiguously computed (for the chosen gauge). We then choose the gauge in B to be aligned to that of A . Assuming this also results in a smooth gauge in B , we could then confidently compute ΔP from Eqs. (3.1) and Eq. (3.8).

3.2.4 Gauge invariant formulation

The procedure described in the last section involved constructing a smooth gauge in A , aligning the gauge in B , and then computing each ϕ_λ via Eq. (3.18). This represents a straightforward, but also inconvenient, means of applying the same gauge class assumption to a realistic calculation. In this section and the next we will develop an equivalent procedure that is more computationally efficient and does not require explicit construction of smooth or aligned gauges.

First, we note that the value obtained above is equivalent to evaluating Φ as

$$\Phi = \sum_i \Delta \mathcal{A}_i \quad (3.20)$$

where

$$\Delta \mathcal{A}_i = \mathcal{A}_i(\lambda_B) - \mathcal{A}_i(\lambda_A) \quad (3.21)$$

is the difference between Eq. (3.19) evaluated at the initial and final configurations (with the previously discussed gauge choices). At present, it is required that k has been sampled densely enough such that each $\Delta \mathcal{A}_i$ is smaller in magnitude than π .

We next note that the quantity $\Delta \mathcal{A}_i$ is equal to the discrete Berry phase computed around the perimeter of the rectangular plaquette marked by the green arrows in Fig. (3.1). To see this, we denote the four corners of this plaquette as $\mathbf{q}_1 = (k_i, \lambda_A)$, $\mathbf{q}_2 = (k_i, \lambda_B)$, $\mathbf{q}_3 = (k_{i+1}, \lambda_B)$, and $\mathbf{q}_4 = (k_{i+1}, \lambda_A)$, and refer to it henceforth as plaquette p located at $k_i = k_p$. Defining the overlap matrices

$$M_{mn}^{(ij)} = \langle u_m(\mathbf{q}_i) | u_n(\mathbf{q}_j) \rangle, \quad (3.22)$$

the four-point Berry phase about the loop, traced over occupied bands, is

$$\phi^p = \text{Im} \ln \det [M^{(12)} M^{(23)} M^{(34)} M^{(41)}]. \quad (3.23)$$

This four-point Berry phase is equal to the Berry flux through the plaquette, by the same Stoke's theorem argument used to relate Eq. (3.2) and Eq. (3.4). This plaquette Berry flux, ϕ_i , can be seen to be equal to $\Delta \mathcal{A}_i$ computed with the gauges specified above since the alignment of gauges insures that $M^{(12)}$ and $M^{(34)}$ have real positive determinants, and

thus don't contribute to the phase being extracted by the Imln operation. The advantage of computing ϕ^p as in Eq. (3.23) is that it is completely insensitive to the gauges used to represent the states at any of the four \mathbf{q}_i [40]. Using Eq. (3.20) we can write Φ as the sum over plaquette Berry fluxes,

$$\Phi = \sum_p \phi^p. \quad (3.24)$$

As the Imln operation suggests, ϕ^p is only gauge invariant up to an integer multiple of 2π , so the above formula still requires that the k -mesh spacing be fine enough that each $|\phi^p| < \pi$ for all k_p , just as was required for ΔA_i .

3.2.5 Berry flux diagonalization

With Eqs. (3.1), (3.23) and (3.24), one can compute the polarization difference using arbitrarily chosen gauges for systems A and B . However, there is still a requirement that the k -mesh be fine enough that all ϕ_p in Eq. (3.24) are smaller in magnitude than π . For a single-band system, this typically does not require a mesh any finer than that needed to compute ϕ_λ from Eq. (3.16). However, the plaquette Berry fluxes ϕ^p from Eq. (3.23) are traced over all occupied bands, so their values can quickly grow much larger in magnitude than π when many bands are contributing.

We can instead decompose each plaquette flux into a sum $\phi_p = \sum_n \phi_n^p$ of smaller gauge-invariant phases ϕ_n^p , where n runs over the number of occupied bands. These are the multi-band Berry phases or Wilson loop eigenvalues of plaquet p , obtained from the unitary evolution matrix \mathfrak{U}_p acquired by traversing the boundary of the plaquette. Explicitly,

$$\mathfrak{U}_p = \mathcal{M}^{(12)} \mathcal{M}^{(23)} \mathcal{M}^{(34)} \mathcal{M}^{(41)} \quad (3.25)$$

where $\mathcal{M}^{(ij)}$ is the unitary approximant of $M^{(ij)}$, that is, $\mathcal{M} = V^\dagger W$ where

$$M = V^\dagger \Sigma W \quad (3.26)$$

is the singular value decomposition of M . The eigenvalues of the unitary matrix \mathfrak{U}_p are of the form $e^{i\phi_n^p}$, providing the needed ϕ_n^p , which are gauge-invariant. Since $\text{Imln det } \mathfrak{U}_p$ is taken as the Berry flux through plaquet p , we have in a sense diagonalized this Berry flux

by obtaining the eigenvalues of \mathfrak{U}_p . Finally, the ϕ_n^p can be summed over all plaquettes to obtain the total polarization difference via

$$\Phi = \sum_p \sum_n \phi_n^p. \quad (3.27)$$

This is our central result.

For the method to be applicable the two states λ_A and λ_B must be similar enough that the singular values in Σ do not become too small (this corresponds to the continuum-case requirement that the norm of γ^{AB} in Eq. (3.11) should remain nonzero). For agreement with the continuum case the individual ϕ_n^p must each be much smaller in magnitude than π . This condition is typically satisfied with a k -mesh density appropriate for a standard Berry-phase polarization calculation, but the density of the k mesh could be increased if necessary. These conditions are further discussed in Section 3.5.3.

The above expressions were all written for the one-dimensional case for the sake of simplicity; the generalization to two and three dimensions is quite straightforward. Just as is typically done for the computation of the Berry-phase polarization, the computation is carried out separately for each string of k -points in the direction of the desired polarization component, and the results are then averaged over the complementary directions.

Note that while the computation of overlap matrices between neighboring k -points is quite routine, this procedure also requires overlaps between wavefunctions of corresponding k -points at different λ values (typically different structures). The implementation details for this procedure are discussed in Sec. 3.3.

3.2.6 Ionic contribution and alignment

Up to this point, we have focused only on computing the electronic contribution to the change in polarization for already fixed choices of unit cells at each λ . Differences in origin choice and cell orientation between λ_A and λ_B can alter the Bloch function overlaps in Eq. (3.17).¹ The berry flux diagonalized method is most robust when structures are

¹Small rotations in going from A to B present no difficulty, since in practice the calculations are done in internal (i.e., lattice-vector) coordinates. For the same reason, a change in strain state presents no difficulties in principle, but can require some attention to the details of indexing of reciprocal lattice vectors.

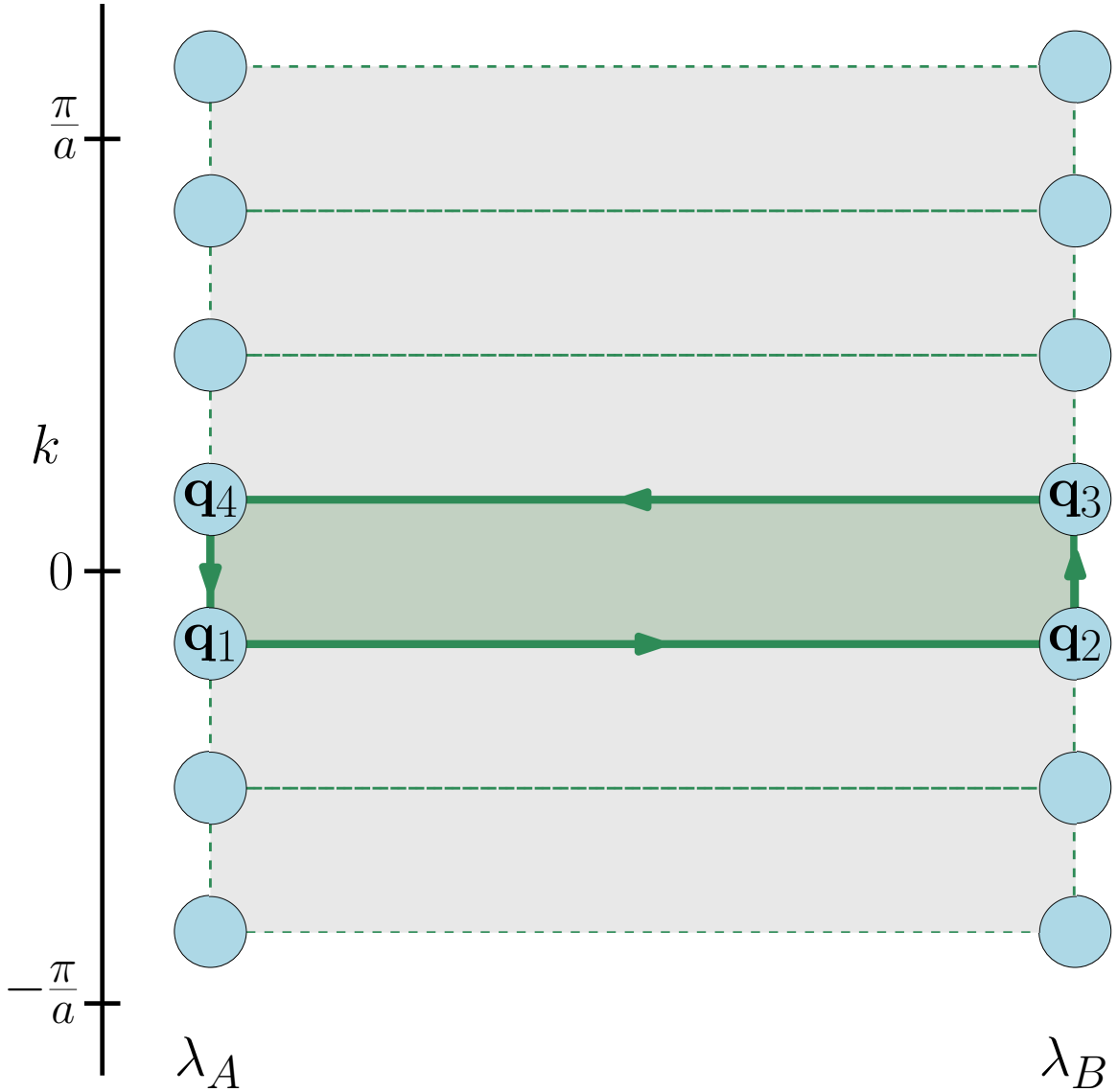


Figure 3.1: Sketch of the joint (k, λ) space for computing a change in polarization between λ_A and λ_B . Blue circles represent points where Bloch wavefunctions have been computed. The light grey box represents the surface S that is integrated over in Eq. (3.2). Dotted green lines represent the plaquets i and the solid green lines represent the path on which the parallel transport procedure is performed around the green plaquet it encloses to obtain its contribution to $P^B - P^A$.

aligned to maximize overlaps, and thus keep elements of the Σ matrix in Eq. (3.26) (the singular values) from becoming too small. We make this choice of unit cell by first aligning the structures to minimize the root mean squared displacements of the ionic coordinates. After this initial alignment, we further refine the choice of origin by translating along the polarization direction to maximize the smallest of all the singular values encountered while scanning over all k -points in the above-described procedure. This additional refinement can be performed without additional first-principles calculations using the existing wavefunctions; in the plane-wave representation this is accomplished by computing

$$M_{mn}^{(AB)}(\mathbf{k}) = \langle \psi_{m\mathbf{k}}^A | T_\tau \psi_{n\mathbf{k}}^B \rangle = \sum_{\mathbf{G}} C_{m,\mathbf{G}+\mathbf{k}}^{(A)*} C_{n,\mathbf{G}+\mathbf{k}}^{(B)} e^{-i\mathbf{G}\cdot\tau}$$

where T_τ is the extra translation by τ and the $C_{n,\mathbf{G}+\mathbf{k}}$ are the plane wave coefficients.

The ionic contribution to the polarization change is given by

$$\Delta \mathbf{P}_{\text{ion}} = \frac{e}{V_{\text{cell}}} \sum_i Z_i \Delta \mathbf{r}_i \quad (3.28)$$

where $\Delta \mathbf{r}_i$ is the displacement of ion i between states λ_A and λ_B .

3.3 Methods

The Berry flux diagonalization method is a post-processing step for wavefunctions generated by first-principles density-functional-theory codes. Our current implementation of the method, available at github.com/jrbp/berry-flux-diag, is for wavefunctions in a plane-wave basis. Here we perform calculations in ABINIT using the norm conserving scalar relativistic ONCVSP v0.3 pseudopotentials with the LDA exchange correlation functional [41]. The necessary overlap matrices are computed from the NetCDF wavefunction files produced by ABINIT, read using the abipy library [42] (<https://github.com/abinit/abipy>). The pymatgen library [25] is used in the process of computing the ionic contribution.

We validate and demonstrate the Berry flux diagonalization method as follows. First, we use the method to compute the switching polarization of the prototypical ferroelectric perovskite oxides BaTiO₃, KNbO₃, and PbTiO₃, for which the computation of the switching polarization by existing methods is straightforward. We then use a $2 \times 2 \times 1$ supercell to

compute the switching polarization of pure PbTiO_3 and of $\text{PbTi}_{0.75}\text{Zr}_{0.25}\text{O}_3$ to demonstrate how difficulties in resolving the branch choice faced by other approaches due to the small polarization quantum do not arise in the Berry flux diagonalization method. The atomic positions in $\text{PbTi}_{0.75}\text{Zr}_{0.25}\text{O}_3$ were taken to be the same as in the pure system.

3.4 Results

The computed switching polarizations for the prototypical ferroelectric perovskite oxides BaTiO_3 , KNbO_3 , and PbTiO_3 are 0.26 C/m^2 , 0.29 C/m^2 and 0.77 C/m^2 respectively, in agreement with the established first-principles literature and experimental observations [43]. In this section, we give a detailed analysis of the results for pure PbTiO_3 , which has the largest polarization and thus presents the most difficult test case. We do this for three cases, namely in the primitive 5-atom cell, in a $2 \times 2 \times 1$ supercell, and in the same supercell but with one Ti replaced by Zr.

The key quantities here are the Wilson loop eigenvalues, which are summed in Eq. (3.27) to obtain the change in polarization. For PbTiO_3 , the distribution of the Wilson loop eigenvalues is shown in Fig. 3.2 for plaquets along the string of k -points corresponding to $k_x = \pi/4a, k_y = \pi/4a$ for the primitive cells, and to the corresponding point $k_x = \pi/2a, k_y = \pi/2a$ for the supercell systems. All Wilson loop eigenvalues are found to be much smaller in magnitude than π , mostly clustered around zero, with a bias in the direction of the electronic polarization change. Here this is negative given the choice of initial and final states.

Each individual contribution to the change in polarization for the supercell is identical to that of the primitive cell, except that they appear with multiplicity four due to the translational symmetries that were lost in the supercell system. So, while the change in dipole moment for the supercell is four times as large as that for the primitive unit cell, and is thus significantly larger than the 2π phase ambiguity, this does not present any difficulties in the Berry flux method.

The Wilson loop eigenvalues for the system with one Ti replaced by Zr is shown in the

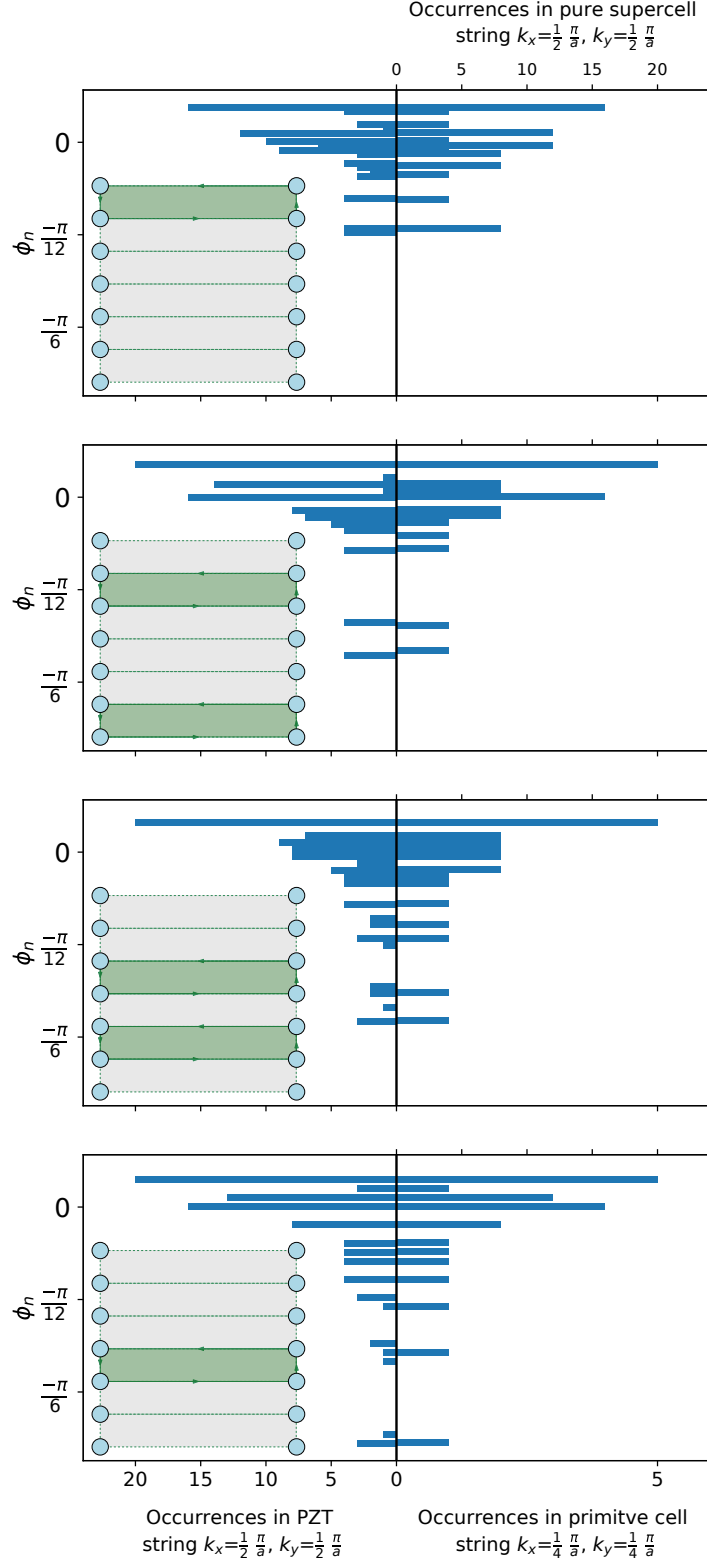


Figure 3.2: Histogram of Wilson loop eigenvalues (ϕ_n^p from Eq. (3.27)) for the plaquets highlighted in the insets following the form of Fig. 3.1. In each of the two middle plots, the two highlighted plaquets have identical contributions due to time reversal symmetry. Values for pure PbTiO_3 are shown on the right. The occurrences of values for the primitive and supercell systems differ only by a factor of 4 as indicated by the two axis scales at the top and bottom of the figure. Values for $\text{PbZr}_{0.25}\text{Ti}_{0.75}\text{O}_3$ are shown at left.

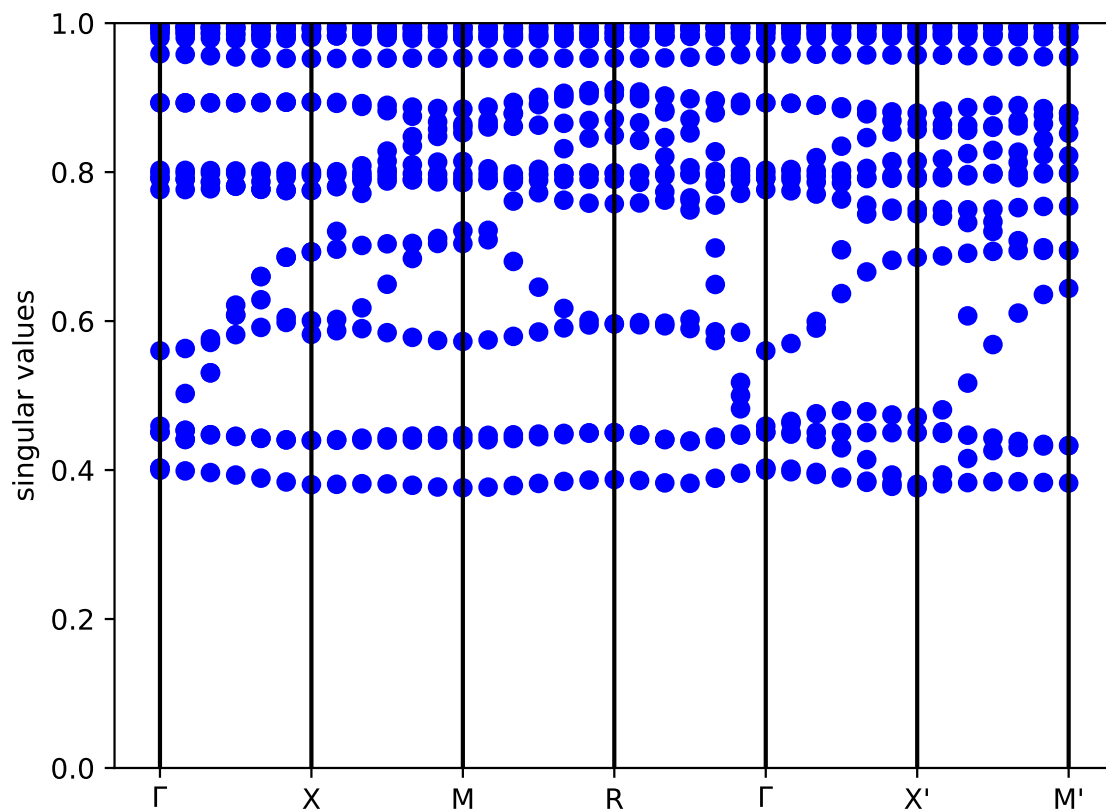


Figure 3.3: Singular values throughout the Brillouin zone for PbTiO_3 , sampled on a $12 \times 12 \times 12$ Γ centered k mesh.

left portion of Fig. 3.2. All eigenvalues fall in the same range as the pure PbTiO_3 system, but with some splitting of values. The switching polarization for the system with Zr was found to be 0.762 C/m^2 compared to the slightly larger 0.771 C/m^2 of the pure system.

In Fig. 3.3, we show the singular values of overlap matrices M between initial and final states at corresponding k -points for PbTiO_3 in its primitive cell. These singular values are the diagonal elements of Σ from Eq. (3.26). If the singular values do not approach zero at any point in the Brillouin zone, the computed information for initial and final states determines the polarization change within the same gauge class assumption. Fig. 3.3 shows that the singular values for PbTiO_3 are well behaved.

3.5 Discussion

3.5.1 Comparison to fictitious path approach

In this section we compare the Berry flux diagonalization method to the commonly used fictitious path approach, using PbTiO_3 in its primitive cell and in a $2 \times 2 \times 1$ supercell as illustration.

For the fictitious path approach, we choose a simple linearly interpolated path between oppositely polarized states. Fig. 3.4 shows the formal polarization which is determined modulo the polarization quantum, computed at points along the path for two different sampling densities. Starting with an arbitrary choice for the initial state, the branch is chosen by connecting to the closest value for the next sampled state along the path. The difference between the final and initial states is then divided by two to get the spontaneous polarization.

For the case of the primitive cell, calculations for three intermediate states on the path are needed correctly to resolve the branch ambiguity. In the case of the supercell, because of the four-fold decrease in the polarization quantum, the number is significantly larger: 15 intermediate calculations must be done to resolve the branch ambiguity. The Berry flux diagonalization approach in both cases, shown by the blue arrow, predicts the change in polarization (with the correct branch choice) using only the wavefunctions in the initial and

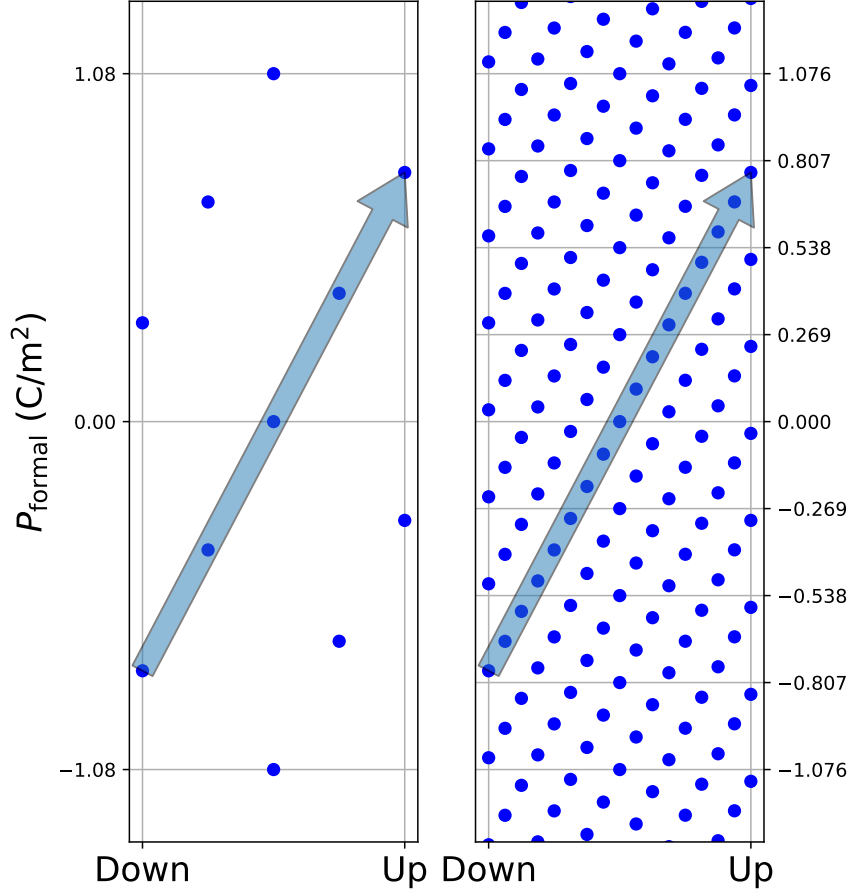


Figure 3.4: Evolution of formal polarization of PbTiO_3 along a linearly interpolated switching path for the primitive cell (left) and a $2 \times 2 \times 1$ supercell (right). Ticks and horizontal lines mark the polarization quantum. The blue arrow indicates the change in polarization, which with the Berry flux diagonalization method only requires calculations in the initial state and symmetry-related final state.

final states.

We note that other approaches have been discussed that utilize partial information in addition the evolution of P_{formal} , such as nominal valence charges and Born effective charges. This additional information can help determine the choice of polarization value at the next point on the path even when this is not the smallest change, reducing the sampling density needed. However, the implementation tends to be ad-hoc and is not suitable for automated high-throughput applications. Furthermore, such approaches may not be reliable in situations where these assumed charges are not constant through the switching process.

3.5.2 Relation to Wannier functions

The Wilson loop eigenvalues ϕ_n^p used in Eq. (3.27) and shown in Fig. 3.2 have a close relation to maximally localized Wannier centers. The parallel transport formalism used to obtain these ϕ_n^p is precisely the same as that used to obtain maximally localized Wannier centers in 1D systems. Such maximally localized Wannier centers are obtained by performing this procedure not across the plaquets discussed in Sec. (3.2.4), but by the loop formed by traversing the Brillouin zone at a given λ . The resulting Wilson loop eigenvalues are then the maximally localized Wannier centers corresponding to a set of Wannier functions (given by their corresponding eigenvectors) which diagonalize the position operator, and sum to compute the formal polarization.

In an analogous way the Wilson loop eigenvalues used in the Berry flux diagonalization method correspond to a set of eigenvectors which diagonalize contributions to a “change in position.” The Wilson loop eigenvalues being used here are summed to compute the change in formal polarization.

3.5.3 Conditions for applicability

To make any branch choice and compute the change in polarization, some assumption about the dynamics of the switching process must be made. In the method presented in this work, the assumption is that the system evolves in some minimal way between oppositely polarized states. Ionic contributions to the change in polarization are separated by assuming displacements are minimized, and electronic contributions are separated by assuming single-particle wavefunctions evolve into those which have maximal overlap across changes in λ . Such assumptions can fail or become difficult to satisfy for certain systems.

This regime where the technique breaks down can be detected automatically. When the changes in the electronic states across changes in λ becomes large, the overlaps in wavefunctions become small, and some singular values of the Σ matrix of Eq. (3.26) approach zero. The implementation of the method checks to make sure that no singular values anywhere in the Brillouin zone fall below a threshold (see Fig. 3.3). Numerical experiments

have shown that a threshold of around 0.15 seems to work well for systems tested. There is of course also a branch ambiguity if the Wilson loop eigenvalues (ϕ_n^p of Eq. (3.27)) have magnitudes close to π . In practice, we have found no cases where this happens without the requirement on the singular values failing first. This can be understood from the viewpoint that the Wilson loop eigenvalues are related to displacements of Wannier centers, with a value of π corresponding to a single charge moving by half a unit cell. When the charge is moved over such a distance the overlaps tend to become small, especially in an insulating system where states are localized. For such systems, one can revert to constructing intermediate states along λ . If each change in polarization is computed using the Berry flux diagonalization method, λ can be sampled more coarsely than methods that track only the total phase. However, in doing so one should beware of making possibly unsafe assumptions about the dynamics of the switching process.

3.6 Conclusion

The Berry flux diagonalization method presented here provides a way to compute the change in polarization that is more easily automated, as well less computationally expensive, than existing approaches. The magnitudes of the singular values obtained in the course of the calculation provide a built-in test that the two systems being compared are sufficiently similar that a class of minimal paths producing the same change in polarization can be inferred. Future work will explore the application of this method to the change in polarization between two states that are not symmetry related, such as in pyroelectrics, antiferroelectrics, heterostructures and insulators in finite electric fields. It will also be interesting to test the applicability of the approach to different classes of ferroelectrics, such as organic, inorganic order-disorder, charge-ordered, or improper ferroelectrics. Generalizations of the method to the computation of other quantities requiring Berry curvature integration, such as Chern numbers and characterization of Weyl points, should also reward future investigation.

Chapter 4

Models: Bulk layer model for superlattices

4.1 Introduction

Ongoing progress in atomic scale precision growth of perovskite oxide superlattices enables exploration of an ever increasing variety of systems.[44, 45, 46, 47] There is particular interest in systems in which the layering gives rise to distinctive functional properties, including enhancement of properties such as the piezoelectric response over those of either constituent [48]. While the microscopic origins of such behavior could include symmetry breaking by artificial structuring, a high density of atomically and electronically reconstructed interfaces, and finite size effects in the unit-cell-scale constituent layers, early experimental and first-principles investigation of BaTiO₃/SrTiO₃ superlattices suggested that the properties of superlattices, even with ultrashort periods, can in fact be largely predicted by a “bulk-layer” model in which the properties of the superlattice are obtained by considering the bulk response to the changes in mechanical and electrical boundary conditions imposed on each constituent layer by lattice matching and approximate polarization matching [49, 50, 51, 52].

For a given constituent material, the bulk response to the changes in mechanical boundary conditions corresponding to lattice matching is readily computed in a first-principles framework via a strained-bulk calculation in which two lattice vectors of the bulk material are fixed to match the substrate at the interface plane, and other structural parameters are relaxed [53, 54]. The development of first-principles methods allowing the calculation of structure and properties in nonzero uniform electric fields [55] and the subsequent recognition of the displacement field \mathbf{D} as the fundamental electrostatic variable [56] allow a quantitative determination of how a constituent layer responds to changes in electrical boundary conditions, including a correct description of nonlinear behavior at high fields.

The use of these nonlinear first-principles electric-elastic constitutive relations enables the model to capture behavior beyond a simple averaging of end point properties.

The bulk-layer model has been successfully applied to a number of perovskite superlattice systems. For $\text{BaTiO}_3/\text{SrTiO}_3$, it accounts for the observed polarization of the SrTiO_3 layers [49, 50] and the evolution of the structure and polarization with epitaxial strain [57, 58, 59]. Extension to the case of perovskite superlattices with “charge-mismatched” constituents (for example, $\text{A}^{3+}\text{B}^{3+}\text{O}_3/\text{A}'^{2+}\text{B}'^{4+}\text{O}_3$) [60] yielded quantitative predictions for the epitaxial strain dependence of the structure and polarization of $\text{PbTiO}_3/\text{BiFeO}_3$ superlattices [60, 61]. A version of the model was also used to study the response of ferroelectric capacitors with metallic electrodes [62]. For a broader range of superlattice systems, the predictions of the bulk-layer model can be expected to provide a good starting point from which interface and finite size effects can be identified and analyzed as contributions from such effects are absent in the model.

In this chapter, we show how to extend this definitive implementation of the bulk-layer model to the prediction of dielectric and piezoelectric responses in insulating superlattices. For three prototypical titanate superlattice systems, $\text{PbTiO}_3/\text{BaTiO}_3$, $\text{BaTiO}_3/\text{SrTiO}_3$, and $\text{PbTiO}_3/\text{SrTiO}_3$, we generate the necessary information about the bulk constituent compounds, apply the bulk-layer model to the prediction of superlattice structure, polarization, dielectric and piezoelectric responses and show that the model can capture the essential trends with composition by comparing to results using first-principles methods of the full superlattices. Thus, using only a database of computed bulk constituent electric-elastic constitutive relations, it should be possible to map out a large configuration space of superlattice combinations and investigate the microscopic origins of their functional properties, leading to a powerful data-driven method to facilitate discovery and design of superlattice systems with enhanced and tunable polarization, dielectric permittivity and piezoelectric response.

4.2 Methods

4.2.1 Bulk-Layer Model

The constituent layers of the superlattice are modeled as strained-bulk materials [53, 54] responding uniformly to the changes in mechanical and electrical boundary conditions produced by the superlattice, specifically lattice matching and absence of free charge at the interface. Here, we consider superlattices epitaxially coherent with a chosen substrate (here, (001) SrTiO₃), so that the lattice matching is implemented by fixing two lattice vectors (here, $\mathbf{a} = (a_0, 0, 0)$ and $\mathbf{b} = (0, a_0, 0)$) to match the substrate at the interface plane. The absence of free charge corresponds to the condition that the displacement field \mathbf{D} be uniform throughout the system [56]. Throughout this work we specialize to tetragonal systems where \mathbf{D} , \mathbf{E} , and \mathbf{P} are along the four-fold axis with magnitudes given by D , E , and P . The case of charge-mismatched constituents can be treated by including fixed interface charges σ as in [60]. For the specified fixed lattice vectors, each constituent material α is described by the electric-elastic constitutive relations $U(D; \alpha)$, $c(D; \alpha)$, $E(D; \alpha)$, and $P(D; \alpha)$ corresponding to the energy per unit cell (taken relative to its minimum value), out-of-plane lattice parameter, electric field, and polarization, respectively. We note that $E(D)$ is related to $U(D)$ through $E(D) = \frac{1}{\Omega(D)} \frac{dU}{dD}$ [56], where Ω is the unit cell volume. For the superlattice consisting of periodic repeats of k layers of unit cell thickness n_i ; $i = 1, \dots, k$, with superlattice period $N = \sum_i n_i$, the total energy is taken as the sum of the energies of the individual layers:

$$U(D) = \sum_i x_i U(D - \sigma_i; \alpha_i) \quad (4.1)$$

where $x_i = n_i/N$ and $\sigma_i = \sum_{j=1}^{i-1} \sigma_{j,j+1}$, where $\sigma_{j,j+1}$ is the fixed interface charge at the interface between layer j and layer $j + 1$, and $\sigma_1 = 0$.

We consider situations in which the voltage drop V across the sample is controlled, with the $V = 0$ short-circuit boundary condition corresponding to the periodic boundary conditions used in first-principles calculations. In practice, we first construct

$$V(D) = \sum_i n_i E(D - \sigma_i; \alpha_i) c(D - \sigma_i; \alpha_i) \quad (4.2)$$

The D that corresponds to the target V is obtained by solving $V(D) = V$ and if there are multiple solutions, then choosing the one that gives the lowest value of $U(D)$. For $V = 0$, this is equivalent to minimizing $U(D)$ with respect to D as in [60]. When the model is solved at $V = 0$, the D which solves the model is precisely the zero field polarization (P) of the superlattice system. This follows from the definition $D = P + \epsilon_0 E$: with zero overall voltage the total external field is also zero and $D = P$. We then construct $c_{\text{tot}}(D) = \sum_i n_i c(D - \sigma_i; \alpha_i)$, $E_{\text{ext}}(D) = V(D)/c_{\text{tot}}(D)$, and the derivatives of each with respect to D , from which we obtain the zero-stress relative permittivity or dielectric constant $\kappa_{33} = \epsilon_{33}/\epsilon_0 = \frac{1}{\epsilon_0} (dE_{\text{ext}}/dD)^{-1}$ and the piezoelectric response $d_{33} = c_{\text{tot}}^{-1} (dc_{\text{tot}}/dD) (dE_{\text{ext}}/dD)^{-1} = g_{33} \epsilon_{33}$ where $g_{33} = c_{\text{tot}}^{-1} dc_{\text{tot}}/dD$. Note that the dielectric and piezoelectric constants used in this work are for fixed in-plane lattice constants (see supplemental material).

The systems examined in this chapter are two-component superlattices with fixed interface charge equal to zero. In this case equations (4.1) and (4.2) reduce to:

$$U(D) = xU(D; \alpha_1) + (1 - x)U(D - \sigma_{\text{int}}; \alpha_2) \quad (4.3)$$

$$\begin{aligned} V(D) = & Nx c(D; \alpha_1) E(D; \alpha_1) \\ & + N(1 - x) c(D - \sigma_{\text{int}}; \alpha_2) E(D - \sigma_{\text{int}}; \alpha_2) \end{aligned} \quad (4.4)$$

where we include σ_{int} for validity for charge-mismatched constituents; in the charge-matched systems considered here, $\sigma_{\text{int}}=0$. As discussed above, the D that corresponds to the target V is obtained by solving $V(D) = V$ and if there are multiple solutions, choosing the one that gives the lowest value of $U(D)$. From this, polarization, out-of-plane lattice constants, and dielectric and piezoelectric responses can be immediately obtained.

4.2.2 First Principles Calculations

We performed first-principles density-functional-theory calculations with the local density approximation (LDA) using the ABINIT package [63, 64, 65]. Norm-conserving pseudopotentials were generated with the Opium code [66, 67]. An energy cutoff of 800 eV was used with a $10 \times 10 \times 10$ Monkhorst-Pack grid to sample the Brillouin zone for 5-atom-unit-cell systems, and equivalent k point densities for the superlattice systems [11]. Structural

relaxations were performed with a force threshold of 10 meV/Å, except for SrTiO₃ fixed displacement field calculations where the slightly polar structure required a stricter convergence of 1 meV/Å. In plane lattice constants are fixed to that of SrTiO₃, here 3.857 Å. For the superlattices, polarization was computed using the Berry phase formalism [18], and dielectric and piezoelectric responses were computed using density functional perturbation theory (DFPT) [68, 69, 70]. The electric constitutive relations for the materials BaTiO₃, PbTiO₃ and SrTiO₃ were computed using fixed displacement field calculations for the five atom unit cell [56]. Convergence issues encountered (and the measures taken to remedy them) in performing the fixed displacement-field calculations are discussed in the supplemental material.

4.3 Results

4.3.1 Electric-Elastic Constitutive Relations

Figure 4.1 shows the electric-elastic constitutive relations for SrTiO₃, BaTiO₃, and PbTiO₃ computed for displacement fields ranging from $D = 0$ to just above the ground state polarization of PbTiO₃ ($D = 0.85$ C/m²). The ferroelectrics BaTiO₃ and PbTiO₃ display a characteristic double well in the energy and a non-monotonic behavior of the electric field with displacement field, consistent with the results for PbTiO₃ shown in [71]. SrTiO₃ displays its characteristically flat energy well and nonlinear evolution of electric field with displacement field [72], which, as we will discuss below, gives rise to very large dielectric and piezoelectric responses for superlattices with large SrTiO₃ fraction. Within our first-principles framework, SrTiO₃ is very slightly polar, with a shallow double well and non-monotonic electric field at small D as shown in the insets of Figure 4.1; the experimental observation that SrTiO₃ is paraelectric down to low temperatures is attributed to the effects of quantum fluctuations [73]. In the bottom panel of Figure 4.1 the derivative of each $E(D; \alpha)$ curve with respect to D is shown. At large D values this derivative begins to decrease in BaTiO₃, indicating an anomalous softening discussed below. The bulk structural parameters, polarization, dielectric permittivity, and piezoelectric response are

tabulated in the supplemental material.

4.3.2 Superlattice Properties

Fig. 4.2a shows the polarization for PbTiO₃/BaTiO₃ superlattices as a function of x , the layer fraction of BaTiO₃. The bulk-layer model shows a bowing below the linear interpolation between pure BaTiO₃ and pure PbTiO₃. The first-principles results show only a very weak dependence on the superlattice period, converging quite rapidly to the model curve with increasing superlattice period for a given x . The x dependence of model tetragonality c/a , where $c = c_{\text{tot}}/N$ shown in Fig. 4.2a is so strongly bowed that it is nonmonotonic. Here too, the first-principles results do not show a strong dependence on the superlattice period and converge quite rapidly to the model curve with increasing superlattice period for a given x . The bulk-layer model response functions ϵ_{33} and d_{33} also show distinctly nonlinear behavior, with a change in curvature at an intermediate value of x as well as non-monotonic behavior for ϵ_{33} . The first-principles results for the response functions show a stronger dependence on the superlattice period, with substantial enhancement over the model and with the shortest-period (small N), PbTiO₃-richest (small x) superlattices displaying enhancement even above the values of each pure constituent. With increasing period, these values converge quite accurately to the model. This is illustrated by the insets, which show that linear extrapolation of the computed responses for $n : n$ superlattices versus $1 - 1/N$ to $N = \infty$ matches the computed model value. This is as expected, since the interface and finite size effects in individual superlattices should become negligible in this limit, and the physics will be dominated by the effects included in the bulk-layer model, which depends only on x and is independent of the total superlattice period.

The results for the BaTiO₃/SrTiO₃ superlattices, shown in Fig. 4.2b, show an upward bowing for the polarization (opposite to that of PbTiO₃/BaTiO₃), and near linearity for the tetragonality as a function of x , the layer fraction of SrTiO₃. The first principles results show weak dependence on the superlattice period. The near-flatness of the energy well $U(D; \text{STO})$, shown in the main part of Fig 1c, leads to the large dielectric and piezoelectric responses in the SrTiO₃-rich (large x) superlattices. As discussed below this same feature of

$U(D; \text{STO})$ also leads to certain deviations from the model curves at large SrTiO_3 volume fraction, including the polarization, and dielectric and piezoelectric responses of SrTiO_3 -rich (large x) superlattices.

Finally, the results for the $\text{PbTiO}_3/\text{SrTiO}_3$ superlattices, shown in Fig. 4.2c, show only slight bowing for the polarization and the tetragonality as a function of x , the layer fraction of SrTiO_3 . The first-principles results show negligible dependence on superlattice period, lying on or very close to the model curves even for the shortest-period superlattices. The dielectric response grows even more rapidly with x than for $\text{BaTiO}_3/\text{SrTiO}_3$ (note the difference in the vertical scale). The piezoelectric response, in contrast, shows a striking suppression below the pure constituent values at intermediate values of x , which is also clearly evident in the first-principles results.

4.4 Discussion

4.4.1 Analysis of Model Results

The bowing in the x dependence of the polarization for all three systems can be understood by considering $x = 0.5$. There, the minimization of $U(D)$ with respect to D requires $dU(D; \alpha_1)/dD = -dU(D; \alpha_2)/dD$, and examination of Fig. 4.1 immediately shows that the value of D , and thus of P , that minimizes $U(D)$ is between the values that minimize the individual $U(D; \alpha_i)$. For the superlattice systems containing BaTiO_3 , the relatively high stiffness of BaTiO_3 around its minimum gives minimal values of D for $U(D)$ that are closer to that of BaTiO_3 (lower than the average D for $\text{PbTiO}_3/\text{BaTiO}_3$ and higher than the average D for $\text{BaTiO}_3/\text{SrTiO}_3$), corresponding to the observed bowings. The low stiffness of PbTiO_3 combines with the flatness of SrTiO_3 to give a minimizing D close to and just slightly below the average, corresponding to the small downward bowing for $\text{PbTiO}_3/\text{SrTiO}_3$.

The deviations from the simple linear interpolation values in the tetragonality (c/a) can be similarly understood by considering $x = 0.5$. In $\text{PbTiO}_3/\text{BaTiO}_3$, the value of c computed at the average D of the two constituents (\bar{D}), that is $0.5(c(\bar{D}; \text{PbTiO}_3) +$

$c(\bar{D}; \text{BaTiO}_3)$) is 4.102 Å, above the linear interpolation value of 4.087 Å. The downward bowing in P , so that the D at $x = 0.5$ is well below \bar{D} , is thus completely responsible for lowering the value of c/a at $x = 0.5$ so far as to lead to the nonmonotonic dependence on x . In contrast, for $\text{BaTiO}_3/\text{SrTiO}_3$ the upward shift of c/a computed at \bar{D} relative to the linear interpolation value is almost equal and opposite in sign to the downward shift due to the smaller bowing of P , so that c/a vs x is almost linear. Finally, for $\text{PbTiO}_3/\text{SrTiO}_3$, the two shifts are comparable in magnitude and both downward, accounting for the observed downward bowing of P .

The dielectric permittivity of the superlattice $\epsilon_{33} = dD/dE_{\text{ext}}$ can equivalently be written in a form where it is expressed in terms of the behavior of individual layers as:

$$\epsilon_{33} = \frac{\sum_i x_i c(D; \alpha_i)}{\sum_i x_i c(D; \alpha_i) \frac{dE(D; \alpha_i)}{dD}} \quad (4.5)$$

The non-monotonic behavior of ϵ_{33} in $\text{PbTiO}_3/\text{BaTiO}_3$, can be partly attributed to an anomaly in the high- D behavior of BaTiO_3 , with a nonlinear softening for $D > 0.6 \text{ C/m}^2$, as can be seen in the (red) BaTiO_3 dE/dD curve in Figure 4.1. This arises from proximity in the energy landscape to a highly-polar supertetragonal phase of BaTiO_3 which has been predicted to be stable at large negative pressure [74, 75]. While the supertetragonal phase is not even metastable under the mechanical and electrical boundary conditions explored, the values of D achieved in the BaTiO_3 layer in superlattices with a large fraction of PbTiO_3 are in this anomalous regime. Similarly large values of D are achieved in SrTiO_3 layers for $\text{PbTiO}_3/\text{SrTiO}_3$ superlattices with low SrTiO_3 fraction. However, as can be seen in the (blue) SrTiO_3 dE/dD curve in Figure 4.1 while dE/dD does begin to soften in SrTiO_3 it never decreases in the relevant range of D . Furthermore, the large permittivity of SrTiO_3 means that the straightforward effect of more of the system being composed of the high permittivity constituent dominates the evolution of ϵ_{33} with x , and any enhancement due to effects on the energy landscape from a supertetragonal phase are comparably negligible. The dielectric susceptibility of $\text{PbTiO}_3/\text{SrTiO}_3$ is seen to increase more rapidly than in $\text{BaTiO}_3/\text{SrTiO}_3$ (notice the difference in scales between the two plots). While there is a contribution from the slight softening of SrTiO_3 at high D , $\text{PbTiO}_3/\text{SrTiO}_3$ is also the

only one of the three systems examined here where one of the constituents has a negative $dE(D; \alpha)/dD$ for a large range of x (see PbTiO_3 in Figure 1b at $D < 0.55$). A negative $dE(D; \alpha_i)/dD$ in the denominator of equation (4.5) increases the susceptibility of the superlattice [76].

The behavior of d_{33} for each system can be understood by first recalling that $d_{33} = \epsilon_{33}g_{33}$. As can be seen in Figure S1 in the supplemental material, each system's $g_{33}(x)$ has a bowing following that of the polarization bowing for reasons analogous to those discussed regarding the tetragonality. In $\text{PbTiO}_3/\text{BaTiO}_3$ the downward bowing of $g_{33}(x)$ is so strong that it is nonmonotonic. When multiplied by $\epsilon_{33}(x)$, which has the previously discussed enhancement, the resulting $d_{33}(x)$ is monotonically decreasing, with a change in curvature. For both $\text{PbTiO}_3/\text{SrTiO}_3$ and $\text{BaTiO}_3/\text{SrTiO}_3$ g_{33} is a monotonically decreasing function of x , while ϵ_{33} is monotonically increasing, but their d_{33} curves exhibit qualitatively different behavior. This can be understood by considering how the slope at any given x relates to the slope and magnitudes of ϵ_{33} and g_{33} :

$$\frac{dd_{33}}{dx} = \frac{d\epsilon_{33}}{dx}g_{33}(x) + \epsilon(x)\frac{dg_{33}}{dx}$$

For both $\text{BaTiO}_3/\text{SrTiO}_3$ and $\text{PbTiO}_3/\text{SrTiO}_3$ the first term is always positive and the second term is always negative. Then d_{33} will have a negative slope in regions where the following is satisfied:

$$\frac{1}{g_{33}}\left|\frac{dg_{33}}{dx}\right|_{\epsilon_{33}} > \frac{d\epsilon_{33}}{dx}$$

For both SrTiO_3 systems $d\epsilon_{33}/dx_{\text{STO}}$ comes to dominate in the large x_{STO} limit resulting in a positive slope at large x . If at $x = 0$ the above condition is satisfied, the slope is initially negative and the resulting curve is nonmonotonic, while if the slope is positive the curve can monotonically increase (as in $\text{BaTiO}_3/\text{SrTiO}_3$). In $\text{PbTiO}_3/\text{SrTiO}_3$ the larger ϵ_{33} of PbTiO_3 (discussed above), combined with the positive curvature of g_{33} for $\text{PbTiO}_3/\text{SrTiO}_3$, results in the above inequality being satisfied for $x = 0$, leading to the nonmonotonic behavior observed in d_{33} in Figure 4.2c.

4.4.2 Comparison With First Principles Results

An implicit assumption of the bulk-layer model is that the structure within each constituent layer is uniform. In the full first-principles calculations, the structure within each constituent layer is free to vary, and in particular, the region near the interface can be different from the layer interior. These additional degrees of freedom, together with interface effects, contribute to the larger responses seen in the full first-principles calculations. This is particularly pronounced in $\text{BaTiO}_3/\text{SrTiO}_3$ and $\text{PbTiO}_3/\text{SrTiO}_3$ superlattices with high SrTiO_3 fraction, for which examination of the structure in the SrTiO_3 layer shows comparatively large variation within the layer, partly accounting for the discrepancies between the full first-principles superlattice values and the model for ϵ_{33} and d_{33} .

In the results presented here, we have considered 5-atom $P4mm$ structures for the constituent compounds and $1 \times 1 \times N$ $P4mm$ structures for the superlattices, allowing consistent comparisons between the bulk-layer model predictions and the first-principles calculations. In fact, both experimental and theoretical investigations of $\text{PbTiO}_3/\text{SrTiO}_3$ superlattices show that oxygen octahedron rotations appear in the lowest-energy phases [77, 78, 79]. For comparison to $\text{PbTiO}_3/\text{SrTiO}_3$ experiments, this model therefore can straightforwardly be extended, as done for the polarization and structure of $\text{PbTiO}_3/\text{BiFeO}_3$ in [60], by laterally enlarging the unit cells to allow rotations when computing the constitutive relations. The construction of a large database of more complete electric-elastic constitutive relations for a variety of constituents and subsequent search for desirable properties and interesting physics will be the subject of future work. More generally, in superlattice systems where the favored tilt pattern changes across the interface, there will be steric constraints arising from the shared oxygens, tending to propagate oxygen tilt patterns across the interface [80]. This interface effect, not included in the bulk-layer model, will be largest for superlattices with the thinnest constituent layers and become negligible in the limit that the layer thickness will become large.

In $\text{PbTiO}_3/\text{BaTiO}_3$, the dielectric permittivity and piezoelectric responses show strong

period-dependent enhancements relative to the bulk-layer model, with the largest enhancements for the shortest period superlattices: 38% in ϵ_{33} for the 1:1 superlattice and 32% in d_{33} for the 2:1 superlattice. For both ϵ_{33} and d_{33} , the highest values at intermediate x are above the values for either constituent. The enhancement over the values predicted by the model signals the contribution of the interfaces, including atomic and electronic reconstruction, and finite size effects. While interfaces and finite size effects appear to significantly enhance these responses the trend captured by the bulk-layer model alone would identify these compositions as a region of interest as ϵ_{33} demonstrated enhancement at the level of the model alone. Detailed comparison with experimental measurements of the system is the subject of paper in preparation.

4.5 Supplementary Material

4.5.1 Determination of electric-elastic constitutive relations

The nonlinear responses of the constituent layers of the superlattice to changes in mechanical and electrical boundary conditions are modeled by electric-elastic constitutive relations $U(\mathbf{D}; \alpha)$, $\mathbf{c}(\mathbf{D}; \alpha)$, $\mathbf{E}(\mathbf{D}; \alpha)$, and $\mathbf{P}(\mathbf{D}; \alpha)$, where U is the energy, \mathbf{c} is the out of plane lattice vector, \mathbf{E} is the electric field, \mathbf{P} is the polarization, and α denotes the constituent material. In this work we consider systems with symmetry such that $\mathbf{D} = (0, 0, D)$, $\mathbf{c} = (0, 0, c)$, $\mathbf{E} = (0, 0, E)$, and $\mathbf{P} = (0, 0, P)$ so that the functions reduce to $U(D; \alpha)$, $c(D; \alpha)$, $E(D; \alpha)$, and $P(D; \alpha)$. To determine these functions in the relevant range of D , we perform first-principles fixed- D calculations as implemented in ABINIT [63, 64, 65]. In this approach the energy is given by:

$$U(D; \alpha) = \min_{\{\mathbf{r}_i\}} \left[E_{\text{KS}}(\{\mathbf{r}_i\}; \alpha) + \frac{\Omega \epsilon_0}{2} (D - P(\{\mathbf{r}_i\}); \alpha)^2 \right] \quad (4.6)$$

where E_{KS} is the Kohn-Sham energy functional, Ω is the unit cell volume, ϵ_0 is the permittivity of free space, and P is the Berry phase polarization [39, 18].

We have found that for structural relaxation at D much different than the spontaneous polarization additional care must generally be taken to successfully converge the calculation. In the fixed displacement field implementation in ABINIT the functional (4.6) is not

minimized directly. Instead the existing routines for performing fixed electric field (E) are utilized (see [56]). During a single step of structural relaxation the ionic structure is fixed while the electronic Kohn-Sham wavefunctions are determined by applying varying E fields so that $E = \frac{1}{\epsilon_0}(D - P)$ is satisfied upon convergence. If the unrelaxed structure is far from the relaxed structure corresponding to the target D , the ABINIT implementation will fail as the relevant E values become so large that the energy functional no longer has a minimum as discussed in [55].

One way to avoid this is by choosing starting structures close to the target structure for a particular D by changing D in small increments and using the structure from the previous step. However, we have found that with a small modification ¹ to the fixed displacement field routines we can avoid this fine-scale incrementing of D , allowing for roughly an order of magnitude increase in efficiency. The modification is to cap the electric field allowed during intermediate ionic steps. This allows the structure to continue to relax towards structures for which P is closer to the target D and the electric field is smaller. At the largest values of D , it might be that the true electric field is larger than the capping value, yielding results in which the electric field in the final structure is equal to the capping value. In this situation either the cap has to be gradually increased (if there is still a minimum of the U function in this range of E) or no result can be obtained for D at and above this value. We have found a capping E field of 5×10^{-3} a.u. (2.57×10^9 V/m) to work well for the materials studied here. Note that even in an implementation where (4.6) was minimized directly a similar issue would still occur in that there would be no minimum in the energy functional for large $D - P$, and a similar limit on the second term in equation (4.6) would need to be imposed for intermediate relaxation steps.

While this capping of the electric field allows for relaxation at D with starting structures which have a relatively large $(D - P)$, another issue can arise if this difference is too large. Since P of a periodic system takes values on a lattice, special care must be taken to choose the correct branch. Since the default behavior is to choose this branch so as to minimize the internal energy, if one starts a calculation fixing D to a value that differs by a polarization

¹suggested by R. E. Cohen

quantum from the spontaneous polarization of the starting structure, the P will stay on the wrong branch. This can be avoided by ramping D from its zero field value using steps smaller than a polarization quantum but still, for these systems, an order of magnitude larger than what would be needed if E were uncapped.

To compute derivatives of the functions U , E , P and c , we use a spline fit to the first-principles calculations. The relation $E(D) = \frac{1}{\Omega(D)} \frac{dU}{dD}$ is satisfied to high accuracy.

4.5.2 First-principles linear-response calculations with epitaxial constraints

The dielectric and piezoelectric responses obtained in the model correspond to the response of the system with in-plane lattice constants fixed to those of SrTiO₃(001), rather than the zero-stress responses designated ϵ_{33} and d_{33} in ABINIT. In this section, we give details on obtaining the reported responses from the quantities provided by ABINIT.

The epitaxially-constrained dielectric permittivity is $(\frac{dD_3}{dE_3})_{\sigma_3=0}$ where σ is the stress in Voigt notation. To obtain $(\frac{dD_3}{dE_3})_{\sigma_3=0}$ from the quantities provided by ABINIT, we note that with the condition that the in-plane lattice constants are fixed, the in-plane stress will change with electric field. We use the thermodynamic relation:

$$\eta_p = S_{pq}\sigma_q + d_{pm}E_m \quad (4.7)$$

where S is the fixed electric field compliance tensor and η is the strain in Voigt notation [81]. With zero in-plane strain ($\eta_1 = \eta_2 = 0$), $\sigma_3 = 0$, and using the tetragonal symmetry of the systems examined in this work we obtain from equation (4.7)

$$\sigma_1 = \sigma_2 = -\frac{d_{13}}{S_{11} + S_{12}}E_3 \quad (4.8)$$

Next we utilize the thermodynamic relation:

$$D_m = \epsilon_{mn}E_n + d_{pm}\sigma_p \quad (4.9)$$

where ϵ is the zero-stress dielectric tensor and $d_{pm} = (\frac{dD_p}{d\sigma_m})_{E=0}$ is the zero-stress piezoelectric tensor, and we differentiate D_3 with respect to E_3 obtaining:

$$\frac{dD_3}{dE_3} = \epsilon_{33} + \sum_i (d_{i3} \frac{d\sigma_i}{dE_3}) \quad (4.10)$$

The $\frac{d\sigma_i}{dE_3}$ are easily obtained from (4.8) and inserted into the above expression to obtain the desired epitaxially-constrained dielectric permittivity:

$$\left(\frac{dD_3}{dE_3}\right)_{\sigma_3=0} = \epsilon_{33} - \frac{2d_{13}^2}{S_{11} + S_{21}} \quad (4.11)$$

Now we turn to the epitaxially-constrained piezoelectric response $(\frac{dD_3}{d\sigma_3})_{E=0}$. To express this in terms of the zero-stress quantities provided by ABINIT, we proceed in close analogy to the discussion for ϵ_{33} above. Note that with in-plane strain fixed, in-plane stress will change as σ_3 is varied. Again using thermodynamic relation (4.7), still with $\eta_1 = \eta_2 = 0$ and tetragonal symmetry, but now with $E_i = 0$ for all i , we can obtain

$$\sigma_1 = \sigma_2 = -\frac{S_{13}}{S_{11} + S_{12}}\sigma_3 \quad (4.12)$$

Making use of the thermodynamic relation (4.9) we differentiate D_3 with respect to σ_3 obtaining

$$\frac{dD_3}{d\sigma_3} = \sum_i d_{i3} \frac{d\sigma_i}{d\sigma_3} \quad (4.13)$$

The desired $d\sigma_i/d\sigma_3$ are easily obtained from (4.12) yielding the epitaxially-constrained piezoelectric response:

$$\frac{dD_3}{d\sigma_3} = d_{33} - \frac{2d_{13}S_{13}}{S_{11} + S_{12}} \quad (4.14)$$

The lowest-energy structure of the superlattice $\text{PbTiO}_3/\text{SrTiO}_3$ includes distortions which we suppress in the current results by imposing tetragonal symmetry. Some modes corresponding to these distortions are actually unstable in some of our superlattices meaning the full dielectric susceptibility matrices can not be computed. However we are only interested in the response to E fields along the out of plane direction. Since the unstable modes all have an oscillator strength of zero along this direction the relaxed-ion zero-stress permittivity elements of interest can still be obtained.

4.5.3 Comparison of linear response and model (finite difference) for bulk constituents

In the DFPT calculations the response of the material to an electric field is computed using derivatives of the wavefunction with respect to the wavevector (\mathbf{k}) in the Brillouin zone

(BZ), which are found by solving a Sternheimer equation at each \mathbf{k} point. In the finite field calculations used to parameterize the model, dependence on the wavefunction on wavevector (\mathbf{k}) across the BZ are instead incorporated through the polarization P term in the energy functional. These two methods converge differently with respect to \mathbf{k} -point sampling and plane wave basis [82, 70] resulting in small differences between the model and DFPT results even for bulk compounds; details are given in table 4.2.

SrTiO ₃ $P4mm$ (99)				
$a = 3.857\text{\AA}, c = 3.864\text{\AA}$				
$P = 0.109 \text{ C/m}^2$				
Sr	1a	0	0	0
Ti	1b	1/2	1/2	0.501
O	1b	1/2	1/2	0.991
	2c	1/2	0	0.490
BaTiO ₃ $P4mm$ (99)				
$a = 3.857\text{\AA}, c = 4.102\text{\AA}$				
$P = 0.412 \text{ C/m}^2$				
Ba	1a	0	0	0
Ti	1b	1/2	1/2	0.517
O	1b	1/2	1/2	0.963
	2c	1/2	0	0.475
PbTiO ₃ $P4mm$ (99)				
$a = 3.857\text{\AA}, c = 4.073\text{\AA}$				
$P = 0.855 \text{ C/m}^2$				
Pb	1a	0	0	0
Ti	1b	1/2	1/2	0.466
O	1b	1/2	1/2	0.903
	2c	1/2	0	0.392

Table 4.1: Computed structural parameters and polarization (P) of each epitaxially constrained constituent material.

4.5.4 Three Component Superlattices

We note that the model can be used with more than three constituent materials. Results for three component superlattices are show below.

SrTiO ₃			
	d_{33}	ϵ_{33}	g_{33}
FF	69.0	510	0.01528
LR	71.5	528	0.01530
diff	2.5	18	0.00002
% diff	3.6	3.4	0.2
BaTiO ₃			
	d_{33}	ϵ_{33}	g_{33}
FF	31.6	38.1	0.0936
LR	30.9	37.2	0.0937
diff	0.7	0.9	-0.0001
% diff	2.3	2.4	-0.1
PbTiO ₃			
	d_{33}	ϵ_{33}	g_{33}
FF	56.8	62.6	0.1026
LR	58.0	63.7	0.1029
diff	1.2	1.1	0.0003
% diff	2.1	1.8	0.3

Table 4.2: Comparison of finite field (FF) and linear response (LR) results for the dielectric permittivity (ϵ_{33}) and piezoelectric responses ($d_{33} = \frac{1}{c} \frac{dc}{dE}$ and $g_{33} = \frac{1}{c} \frac{dc}{dD}$) of each epitaxially constrained material.

4.6 Conclusions

In summary, we have extended the first-principles bulk-layer model, which predicts the properties of superlattices from the bulk constituent responses to changing mechanical and electrical boundary conditions, to the prediction of dielectric and piezoelectric responses in insulating superlattices. We have presented a quantitative comparison between the model and full first-principles calculations for three sets of superlattices (PbTiO₃/BaTiO₃, BaTiO₃/SrTiO₃ and PbTiO₃/SrTiO₃) demonstrating that the model provides an excellent first approximation to the polarization, tetragonality, dielectric permittivity and piezoelectric response of these systems allowing the identification of interface and finite-size effect contributions. Expansion of the constituent database will allow the efficient exploration of a large configuration space of superlattices, enabling the data-driven design and discovery of superlattice materials with targeted functional properties.

This work is supported by NSF DMR-1334428 and Office of Naval Research N00014-17-1-2770. Part of this work was performed at the Aspen Center for Physics, which is supported

by NSF PHY-1607611. We thank Valentino Cooper, Cyrus Dreyer, Don Hamann, Janice Musfeldt, David Vanderbilt, and Tahir Yusufaly for useful discussions. We also thank Ron Cohen for suggesting the modifications to the fixed displacement field implementation discussed in the supplemental material. Computing resources were provided by the ERDC DoD Supercomputing Resource Center.

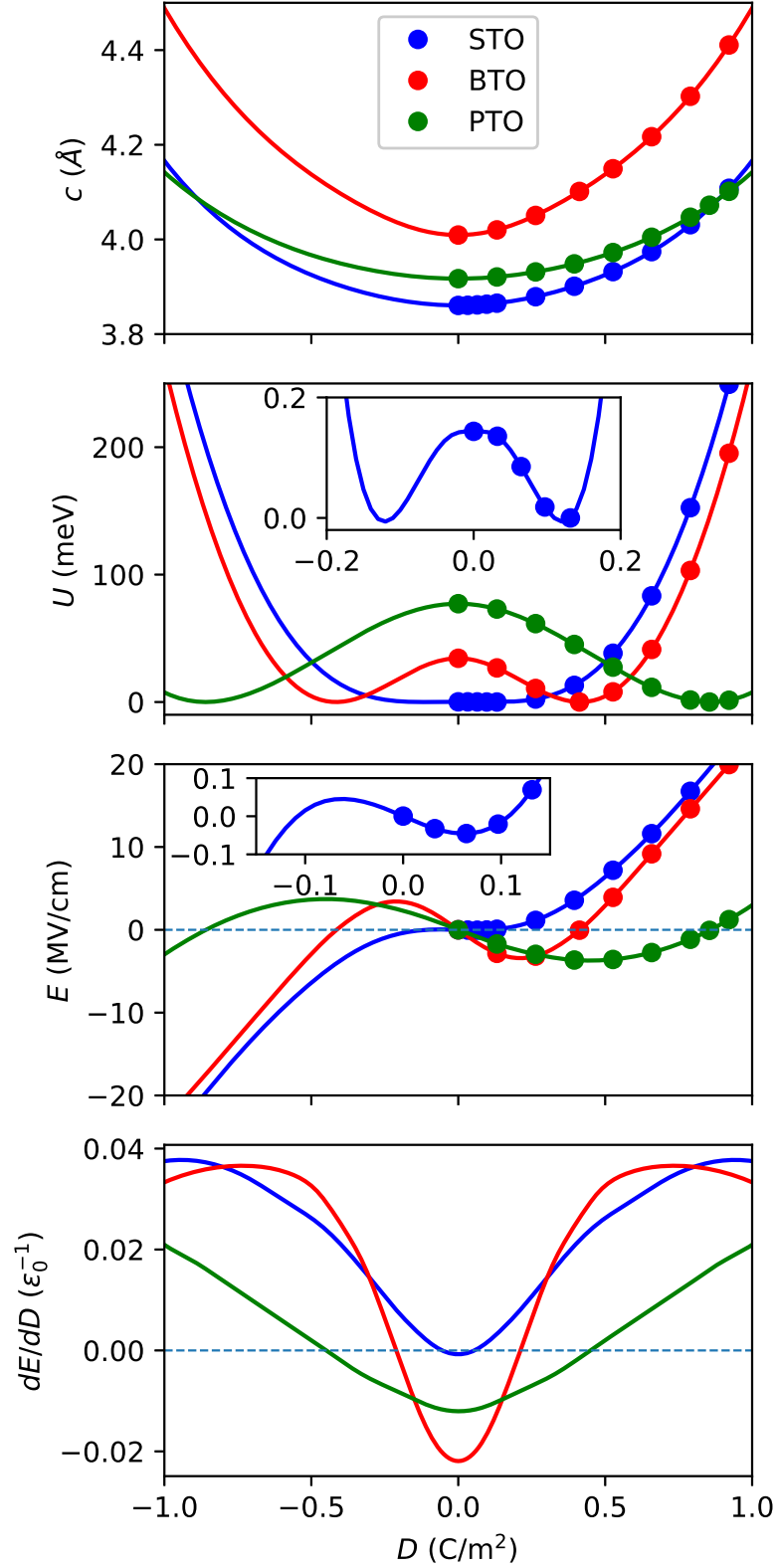


Figure 4.1: Computed electric-elastic constitutive relations for SrTiO₃, BaTiO₃, and PbTiO₃. Filled circles show the calculated values and the solid curves are spline fits. The definite parity of each function is used to obtain the results for negative D . The insets zoom in on the slight polar instability computed for SrTiO₃. The bottom figure shows the derivatives of the spline fits shown in the E plot with respect to D .

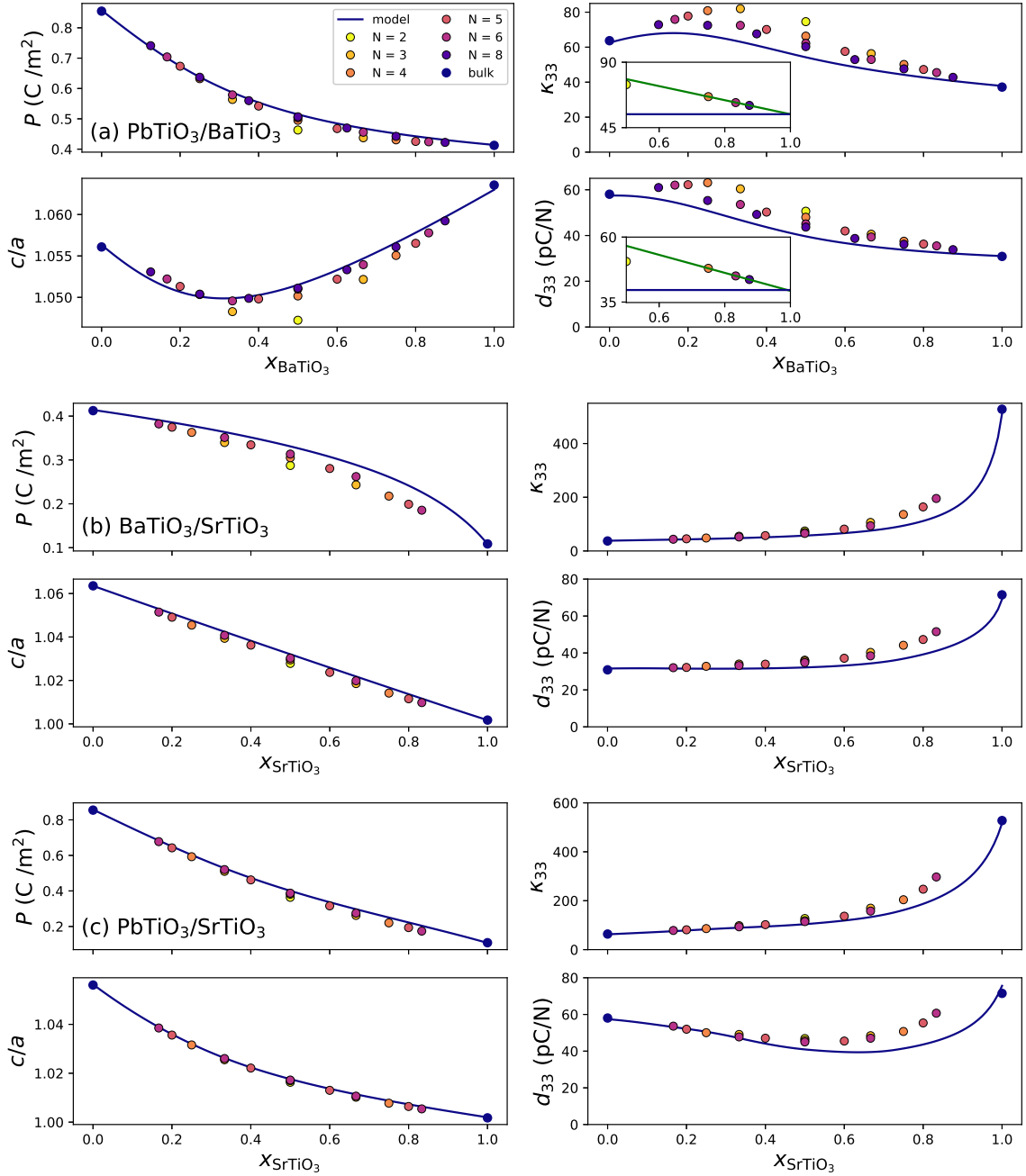


Figure 4.2: Spontaneous polarization, tetragonality (c/a), dielectric response κ_{33} and piezoelectric response d_{33} for (a) PbTiO₃/BaTiO₃, (b) BaTiO₃/SrTiO₃ and (c) PbTiO₃/SrTiO₃, plotted as functions of the layer fraction x of the lower polarization constituent. The bulk-layer model results are shown by a solid line and the first-principles results for individual superlattices are shown as circles filled by colors corresponding to the total superlattice period. The insets in the panels for κ_{33} and d_{33} of PbTiO₃/BaTiO₃ show the first-principles values for $n:n$ superlattices ($x = 0.5$) plotted against $(1 - 1/N)$, where N is the superlattice period in layers of bulk unit cells, with a linear fit to the $N > 2$ values showing accurate convergence to the model value (indicated by the horizontal line). The differing scales of the vertical axes in each figure are chosen to accommodate the differing ranges over which properties vary between systems. The imperfect agreement between the end points and the model is discussed in the supplemental material.

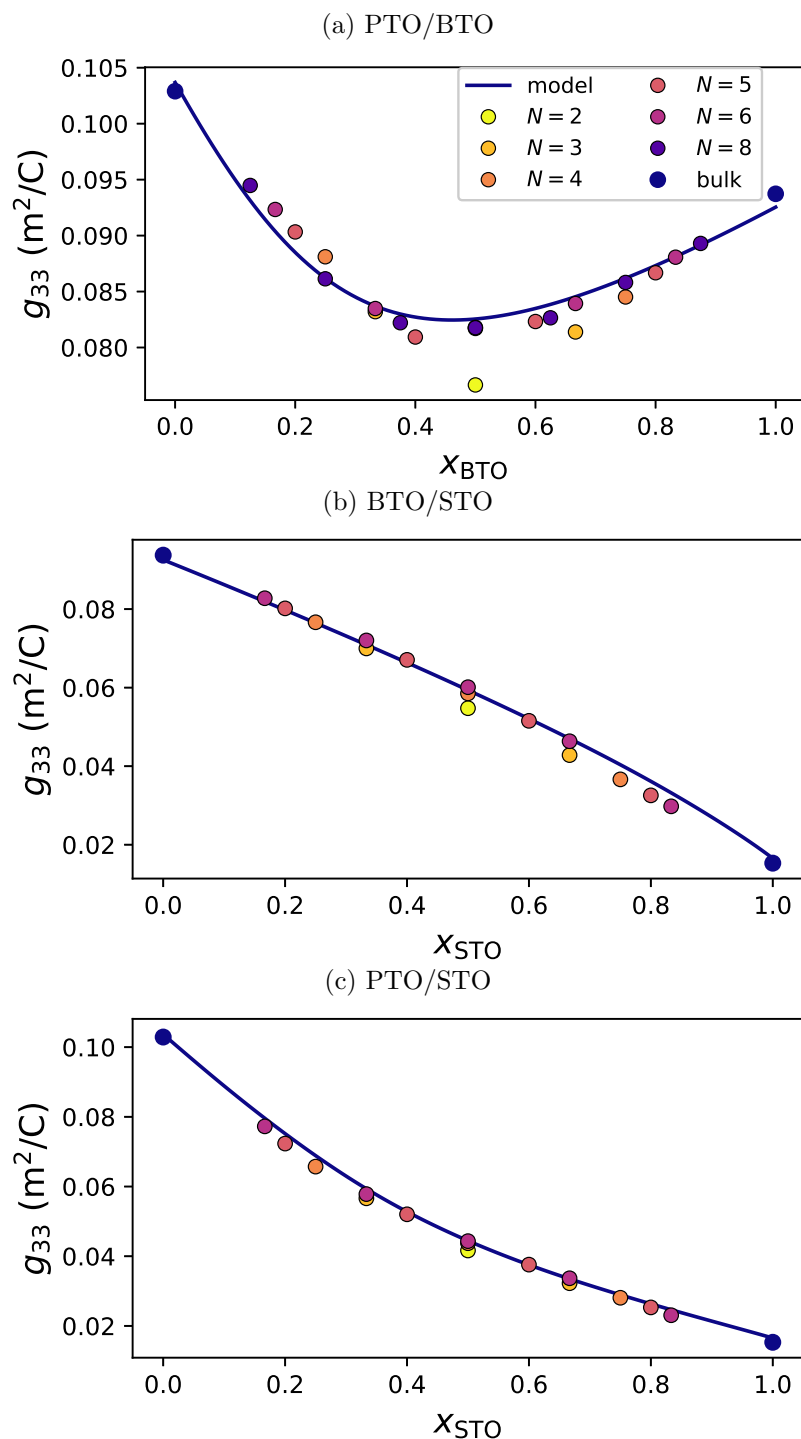


Figure 4.3: Model and first principles results for $g_{33} = \frac{1}{c} \frac{dc}{dD}$ for (a) PTO/BTO, (b) BTO/STO, and (c) PTO/STO as functions of layer fraction x of the lower polarization constituent. The bulk-layer model results are shown by a solid line and the first-principles results for individual superlattices are shown as circles filled by colors corresponding to the total superlattice period.

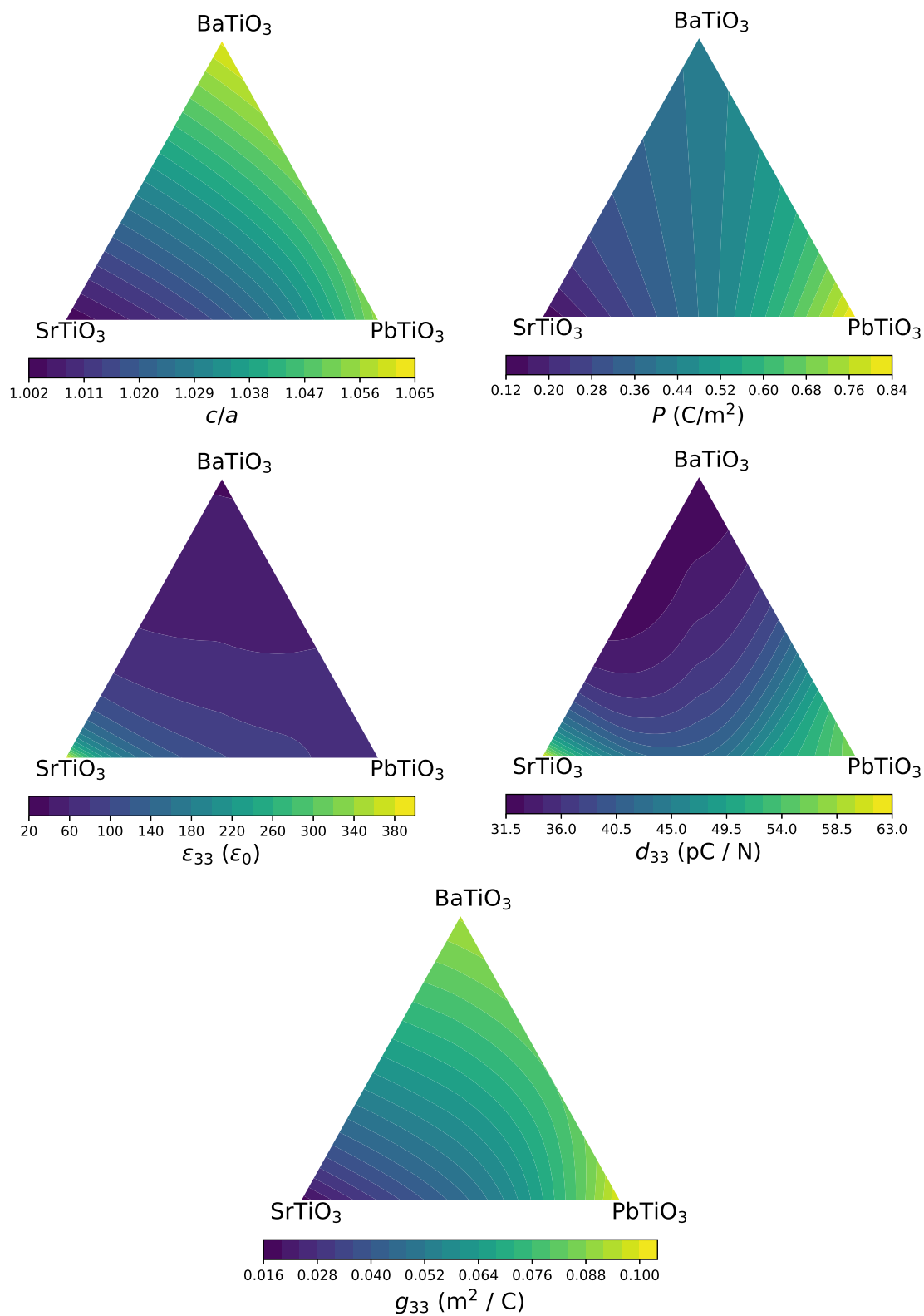


Figure 4.4: Results for three component superlattices

Chapter 5

Tools: Integration of first principles calculations, databases, and group theoretical methods

5.0.1 Introduction

Group theoretical approaches have long been a vital tool in the study of crystal structure. Symmetries can be used to dramatically reduce computational cost. The infinite number of potential structures can be classified into a finite number of space groups. Phase transitions can be modeled by the change in space group along with an order parameter which is defined by an irreducible representation of the higher symmetry space group. In the Landau theory of phase transitions the free energy of a system can be written as a polynomial where each term is a product of these order parameters that is invariant under the high symmetry group operations[83]. The irreducible representations and their corresponding order parameters can be used to construct symmetry adapted distortion modes which, for structures that can be represented as a low-symmetry distortion of some higher-symmetry parent structure, form a complete basis to describe the lower-symmetry structure. Since it is often the case that few of these symmetry adapted modes are active, the basis of these modes can provide an enormous dimensional reduction in exploring and understanding a structure compared to a list of atomic positions in Cartesian or lattice vector coordinates [84].

While group theory is incredibly powerful the 230 spacegroups, the many representations of each, and their application to tens to hundreds of atoms can in practice be impractical for a human to analyze manually. Because of the tedious and error prone nature of applying these techniques by hand, tools which automate portions of this process have become vital. Over the last thirty years Dorian Hatch and Harold Stokes have developed software for applying group theoretical methods to crystalline solids in the ISOTROPY software suite

[85, 86, 87]. The Bilbao crystallographic server has provided its own set of programs for applying group theory methods to crystal structures. These have become essential tools in many researchers workflows and are cited in thousands of papers.

The full potential of these tools can be realized when integrated with existing materials databases and first principles computation software. With this in mind the pysotropy python library was developed as an interface between pymatgen and ISOTROPY. Pymatgen is a python library for materials analysis which powers the Materials Project. Pymatgen provides classes for the representation and analysis of crystal and electronic structure with input and output support for first principles codes such as VASP and ABINIT as well as integration with the Materials Project database API. The integration between python, first principles codes, and databases has enabled large scale high throughput calculation of the properties of many both existing and hypothetical materials. The introduction of the group theoretical tools from ISOTROPY in to this ecosystem unlocks new possibilities in materials design.

Section 5.0.2 demonstrates some of the basic functionalities of the pysotropy library. The pysotropy tool set has enabled automated analysis of thousands of structures from the materials project database to map out group-subgroup relations and the corresponding irrep(s) and symmetry adapted modes which relate them. In section 5.0.3 it is demonstrated that this analysis can be used to classify many related structures in an automated fashion using the pysotropy library.

5.0.2 Pysotropy functionality

The pysotropy library preforms group theory analysis on crystal structures where the input and output data consist of pymatgen structures and native python objects. This allows structure data to be pulled from first principles codes or databases used as input to pysotropy, and the output of pysotropy can be used in further pysotropy analysis, or to start a first principles calculation all in an automated fashion. The core features of pysotropy are available in other tools, but typically in online interfaces such as the Bilbao crystallographic server[34] and the ISOTROPY software suite[36]. Such tools require manual intervention

or clunky web scraping to integrate them with data from first principles codes and material databases. By performing these tasks locally many calculations can be run rapidly without overloading the servers of these services. In this section we demonstrate some of the basic capabilities.

high_symmetry_structure $a = 4\text{\AA}$			
Sr	0	0	0
Ti	1/2	1/2	1/2
O	1/2	1/2	0
	1/2	0	1/2
	0	1/2	1/2

Table 5.1: High symmetry cubic perovskite structure.

low_symmetry_structure $a = 4\text{\AA}, c = 8\text{\AA}$			
Sr	0	0	0
Sr	0	0	1/2
Ti	1/2	1/2	0.2
Ti	1/2	1/2	0.8
O	1/2	1/2	0
	1/2	1/2	1/2
	1/2	0	0.28
	1/2	0	0.72
	0	1/2	0.28
	0	1/2	0.72

Table 5.2: A lower symmetry perovskite structure which can be expressed as a distortion of the structure in table 5.1

One can find which symmetry adapted distortion modes relate a structure to a given high symmetry reference structure. The distorted structure must be in a spacegroup which is a subgroup of the spacegroup of the reference structure. As an example consider the reference structure to be the cubic perovskite structure in table 5.1 (spacegroup $Pm\bar{3}m$) and the distorted variant in table 5.2 (spacegroup $P4/mmm$). Passing these structures to the pysotropy function `get_mode_decomposition` will determine the spacegroup and occupied Wyckoff positions of each structure, find the supercell for the high symmetry structure with the appropriate origin which best matches the distorted cell, find the symmetry adapted distortion modes which are compatible with this information, and project the displacements

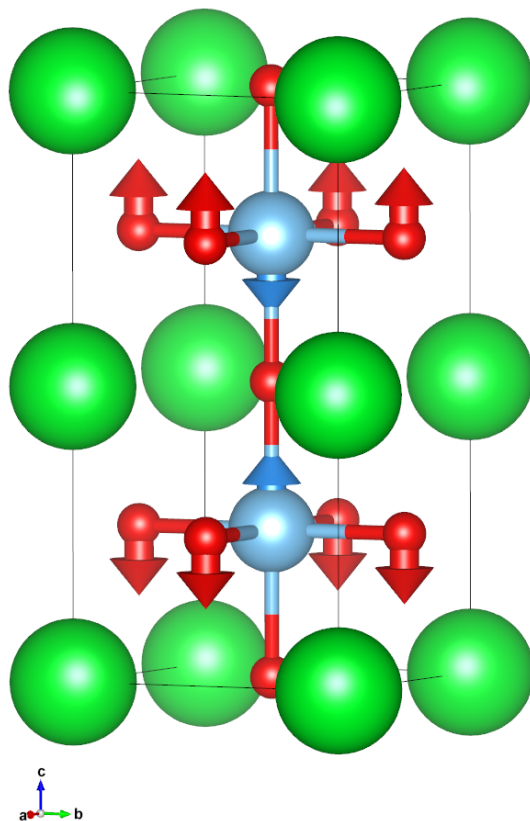


Figure 5.1: Supercell of the cubic perovskite structure given in table 5.1. Arrows indicate the displacements which form the distortion mode of Irrep $X1+$ along the $0, 0, a$ direction leading to the structure in table 5.2.

on to these modes. The mode irreps, directions, definitions, and amplitudes are then returned. For these example structures the resulting mode information is given in table 5.3. The irrep is $X1+$, this is in general a three dimensional irrep (as there are three X points), however this distortion is along only one of these directions, $0, 0, a$. For each Wyckoff position this distortion acts on an amplitude is given as well as a definition listing sites in the high symmetry supercell in fractional coordinates and the direction they are displaced.

One can also work in the other direction by starting with only a high symmetry structure and then choosing a specific mode to freeze in at a given amplitude to obtain a distorted structure. For example, if we are interested in studying K point distortions of graphene

Irrep: X1+						
Direction: (0, 0, a)						
Wyckoff: b0						
Amplitude: 0.56569						
Species	Site			Vector		
Ti	1/2	1/2	1/4	0	0	1
Ti	1/2	1/2	3/4	0	0	-1
Wyckoff: c1						
Amplitude: -0.48						
Species	Site			Vector		
O	0	1/2	1/4	0	0	1
O	0	1/2	3/4	0	0	-1
O	1/2	1/2	0	0	0	0
O	1/2	1/2	1/2	0	0	0
O	1/2	0	1/4	0	0	1
O	1/2	0	3/4	0	0	-1

Table 5.3: Distortion mode definitions and amplitudes that related the structures in tables 5.1 and 5.2

with an out of plane component. We can start with the high symmetry phase of graphene in spacegroup $P6/mmm$ (191) with the 'd' Wyckoff position occupied. Next all irreps at the K point can be found by calling the function `get_irreps(191,kpoint='K')` corresponding distortions obtained by looping through the results and calling the function `get_distortion(parent=191,wyckoffs=['d'],irrep=this_ir)`. We can filter for those with out of plane components and see that only the $K6$ irrep contains any out of plane distortions. This is a four dimensional irrep and we can see how the possible order parameter directions lower the symmetry as shown in table 5.4. The vector pointing the direction of site displacement for each of these four components is given in table 5.5. These distortions can then be frozen in at some amplitude. The resulting structures can easily be exported to cif files for sharing and visualization or to first principles codes to compute properties.

5.0.3 Application: Identifying most common perovskite structures in the Materials Project database

The perovskite crystal structure can exhibit numerous functional properties such as ferroelectricity, piezoelectricity, magnetoresistance, photovoltaic and more. These systems

Direction				Subgroup
0	0	0	a	P321 (150)
0	a	0	0	P31m (157)
0	0	a	a	C222 (21)
0	0	a	-a	C2/m (12)
a	a	0	0	C2/m (12)
a	-a	0	0	Cmm2 (35)
0	a	0	b	P3 (143)
0	0	a	b	C2 (5)
a	b	0	0	Cm (8)
a	a	b	b	C2 (5)
a	-a	b	b	P2 (3)
a	a	b	-b	P-1 (2)
a	-a	b	-b	Cm (8)
a	b	c	d	P1 (1)

Table 5.4: Possible order parameter directions of the $K6$ irrep distortion mode and the resulting lower symmetry space group for graphene.

Point			component 1			component 2			component 3			component 4		
1/3	2/3	1/2	0	0	0	0	0	1	0	0	0	0	0	0
2/3	1/3	1/2	0	0	0.500	0	0	0	0	0	-0.866	0	0	0
4/3	5/3	1/2	0	0	0	0	0	-0.500	0	0	0	0	0	0.866
4/3	2/3	1/2	0	0	0	0	0	-0.500	0	0	0	0	0	-0.866
-1/3	1/3	1/2	0	0	0.500	0	0	0	0	0	0.866	0	0	0
2/3	4/3	1/2	0	0	-1	0	0	0	0	0	0	0	0	0

Table 5.5: Components of the general $K6$ distortion mode which with all components active mixes distortions from multiple K points.

exhibit this large range of functional properties in part because there are many closely related competing distortions possible in the perovskite structure. One can use a combination of pycnometry and the materials project database to see which distortions actually exist in known perovskites, and which combinations of distortions occur most often. From this analysis a set of prototype perovskite structure types can be found by grouping together structures which contain the same distortion modes. Knowledge of the set of distinct closely related structures could be utilized as part of a new efficient approach for structure determination and searching for realizable metastable states as this set of structures are likely to contain low energy minima. Note that utilizing space groups alone is not enough to distinguish between structures, as more than one inequivalent structure can exist in the same

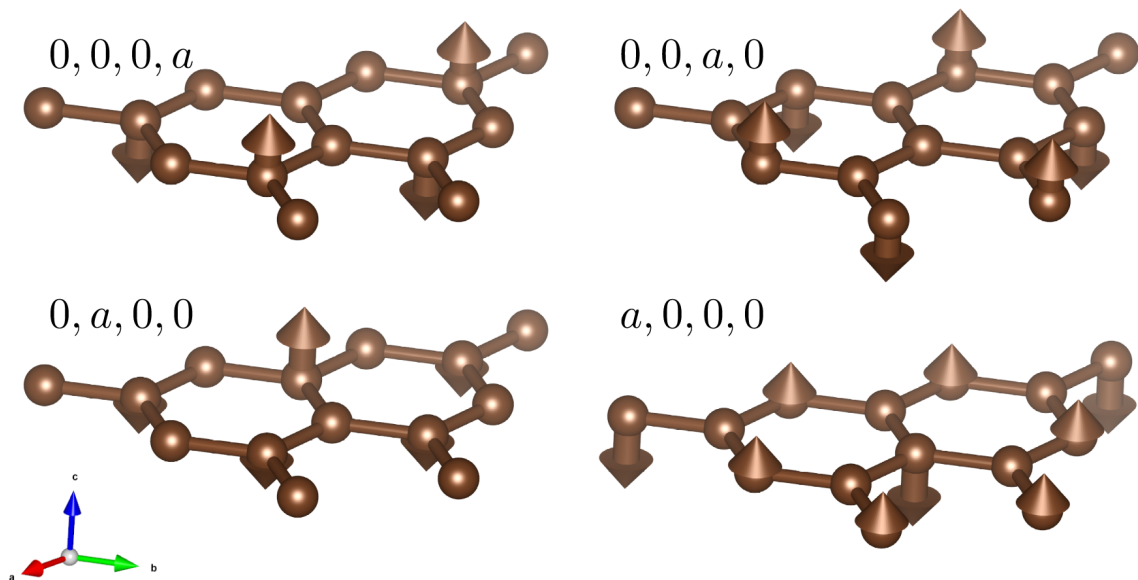


Figure 5.2: Components of the K6 graphene distortion corresponding to those in table 5.5. The K6 order parameter can be viewed as a four dimensional vector which describes the distortion as a linear combination of the distortions shown. Directions of this vector and the symmetries that result are given in table 5.4.

spacegroup (see the $I4/mcm$ structures in table 5.6). Previous approaches to analyze materials databases to classify perovskite structures focused on a subset of distortion modes such as octahedra rotations[88]. Here we make use of all possible distortions, our categorization is determined by how structures are grouped in the database rather than being predefined, and the procedure can be applied to other classes of materials outside of the perovskite family with the choice of some other high symmetry reference structure. This section will serve as a demonstration of how pysotropy can be used as well as illustrating the power of combining the group theoretical tools of ISOTROPY with the Materials Project database in an easily automated framework.

Our strategy was as follows:

1. Use the materials project database and api to obtain all experimental structures which may be perovskites based on stoichiometry
2. Use pymatgen to filter out all structures which require atomic displacements which are above a threshold to relate to the cubic perovskite structure

3. Use pysotropy to characterize all structures by the symmetry adapted distortion modes which related them to the cubic structure
4. Group together structures which contain the same set of modes as examples of the same prototype structure

Using the materials project api we can easily obtain all structures with the stoicheometry ABC_3 .

```
from pymatgen.ext.matproj import MPRester
a = MPRester(api_key)
single_perov_stoich = a.query({'anonymous_formula': {'A': 1, 'B': 1, 'C': 3}},
                             ["material_id", "final_structure"])
```

This downloads over 4000 structures which we can than filter using pymatgen for those closely related to the cubic perovskite structure.

Using the pymatgen library we can work directly with the structures returned by the above query to find the minimal displacements required to relate each structure to the cubic variant. We then filter out structures with displacements so large they can not reasonably be considered perovskites. This produces a list of over 450 perovskite related structures.

Next we use pysotropy to identify the symmetry adapted modes which relate each structure to the cubic perovskite. The pysotropy library contains the module pysodistort which works directly with the pymatgen structures we obtained from the materials project and filtered with pymatgen.

```
import pysodistort as pd
# find mode decomposition which relates two structures:
decomp_data = pd.get_mode_decomposition(cubic_perov, struct)
```

We simply loop over all structures to obtain the symmetry adapted modes and their associated amplitudes which relate them to the corresponding cubic structure for all experimentally known perovskites in ICSD.

We then easily group together structures with the same sets of symmetry adapted distortions and sort them by the number of database entries in each group. As can be seen from Table 5.6 90% of perovskites fall in to one of just 25 prototype structures. In this table

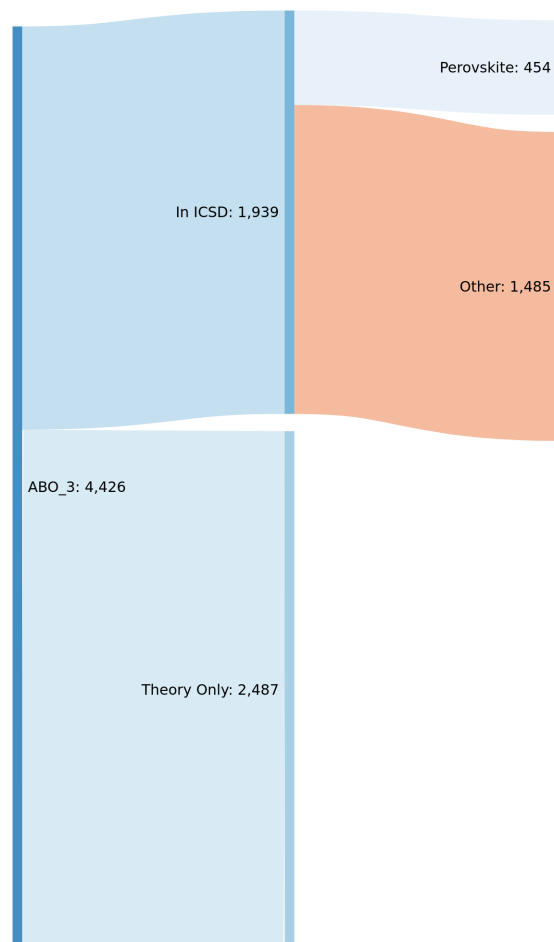


Figure 5.3: Narrowing down structures in materials project from those which satisfy the ABC_3 stoichiometry to those which have been seen experimentally and are small distortions of the cubic perovskite structure.

all modes present in the structure are listed. Typically a subset of these form the primary order parameter which lowers symmetry enough that other secondary order parameters require no additional symmetry breaking. It is not in general possible to identify the unique primary order parameter from structural information alone [89].

Defining a perovskite structure prototype by the symmetry adapted distortion modes present is not a unique choice. This definition specifies which symmetries are present, which Wyckoff positions are occupied, and is invariant under changes in origin since these are set by the chosen high symmetry structure. Since typical first principles relaxation methods preserve the space group of the starting structure it is advantageous that for a given material in a given prototype the low energy mode amplitudes can be found without

#	sg	modes
204	Pnma	(M2+, P1), (X5-, P1), (R4-, P2), (M3+, P1), (R5-, P2)
26	R3c	(R5-, P3), (GM4-, P3)
25	Pm $\bar{3}$ m	
20	I4/mcm	(R5-, P1)
20	R $\bar{3}$ c	(R5-, P3)
17	R3m	(GM4-, P3)
15	P4mm	(GM4-, P1)
14	Imma	(R5-, P2), (R4-, P2)
9	Pna2 ₁	(X5+, P1), (M2+, P1), (X5-, P1), (R4-, P2), (GM4-, P1), (R5-, P2), (M3+, P1), (R5+, P2)
8	P2 ₁ /c	(M2+, P1), (R2-, P1), (X5-, P1), (R3-, P1), (M5+, P10), (R4-, C2), (M3+, P1), (R5-, P2)
7	P4/mbm	(M2+, P1)
5	I4/mcm	(R3-, C1)
4	I4/mmm	(R2-, P1), (R3-, C1)
4	P2 ₁ /c	(M2+, P1), (X5-, P1), (R4-, P2), (M5+, P10), (M3+, P1), (R5-, C2), (X3-, P1), (R3-, P2)
4	Amm2	(GM5-, P2), (GM4-, P2)
4	Cmcm	(M1+, P1), (M2+, P1), (R5-, P1), (X5-, P2), (R4-, P1)
3	P $\bar{1}$	(M1+, P1), (X5-, C1), (M2+, P1), (R2-, P1), (M5+, C13), (R4-, S1) (M4+, P1), (M3+, P1), (X3-, P1), (R5-, S1), (R3-, C1)
3	C2/m	(R5-, P2), (R2-, P1), (R3-, C1), (R4-, C2)
2	P1	(GM4-, P2), (GM5-, C1), (R4-, S1), (R5-, C2), (R5+, S1), (R3-, C1)
2	P2 ₁ /c	(M2+, P1), (X5-, P1), (R3-, P1), (M5+, P10), (R4-, C2), (M3+, P1), (R5-, P2)
2	R $\bar{3}$	(R5-, P3), (R2-, P1), (R4-, P3)
2	Pmc2 ₁	(X1+, P1), (M2+, P1), (X5-, P1), (M5-, P1), (GM5-, P2), (R4-, P2), (M3+, P1), (R5-, P2), (GM4-, P2)
2	Pbam	(X1+, P1), (M5-, P1), (SM2, P2), (R4-, P2), (R5-, P2), (S2, P2)
2	Fm $\bar{3}$ m	(R2-, P1)
2	P4/mbm	(M3+, P1)
33	other	other

Table 5.6: Perovskite structure prototypes with ICSD entries in materials project and their associated spacegroup and symmetry adapted distortion modes from the cubic (Pm $\bar{3}$ m) structure sorted by number of entries present in the database. The Irrep symbol is given along with a symbol specifying the order parameter direction. The symbols for the order parameter directions were chosen by Stokes and Hatch, and are a way of classifying equivalent directions. The final row indicates the 33 structures for which only one example of that structure type is present.

breaking additional symmetry. This makes the prototype structures described excellent choices of starting structure when examining the energy landscape of a particular material. However, it is still possible for multiple metastable states to exist within a given prototype. One example of this occurs in strained PbTiO_3 and BiFeO_3 ; the ordinary tetragonal polar distortion coexists with a metastable supertetragonal phase which involves the same distortion mode, but at a much larger amplitude [75]. A potential refinement of the above prototype structures could further separate each prototype based on the amplitudes of the modes present. One approach would be to apply unsupervised learning algorithms to the distribution of mode amplitudes to find clusters in mode amplitude space which inform ranges of amplitudes which can be grouped in to distinct sub-prototype structures. A challenge in the application of such an approach is that for the majority of the prototype structures there are not enough representative materials in the database for such algorithms to be effective. It is possible that additional first principles calculations with both real and hypothetical structures can provide enough data for this approach to be viable.

Chapter 6

Conclusions and outlook

In this thesis methods, models, and tools to facilitate the computational design of functional materials were developed and applied. Further extensions and applications of these techniques are worthy of investigation to facilitate the design and discovery of materials with novel physics and useful device applications.

In chapter 3 we developed a new theoretical foundation and computational methodology to compute changes in polarization, which was then applied to several well known ferroelectrics. This method breaks down changes in polarization in to separable gauge invariant contributions, allowing changes to be computed in a manner which is more easily automated and with roughly an order of magnitude less computational cost. Future work will entail applying this method to large databases of potential ferroelectrics to identify high quality candidates. The theoretical foundation of this method can be generalized and applied to other Berry curvature integrals. Application of the technique to the computation of quantities besides changes in polarization such as topological invariants and characterization of Weyl points is worthy of investigation.

In chapter 4 a model for obtaining piezoelectric and dielectric responses of superlattice systems from data computed using only the bulk constituents was developed and applied. This method could be applied to a database of many bulk compounds each characterized as a function of displacement field, strain, and other parameters to rapidly identify superlattices with interesting or desirable properties. These properties may involve enhancement of responses as was shown for $\text{PbTiO}_3/\text{BaTiO}_3$. The model can also be used to identify systems where the electrostatic interaction between layers of the superlattice leads to the stabilization of states which are otherwise metastable. The pysotropy software and its

integration with the materials project database presented in chapter 5 can be used to identify close in energy states that may be stabilized in this way.

In chapter 5 we present the pysotropy library for automated group theory based analysis of crystal structures integrated with first principles codes and materials databases. This automation and integration is a powerful tool with numerous applications in the study of materials. For materials which are closely related the mode description of a structure is a basis choice which offers a significant dimensional reduction compared to a list of atomic positions. We utilized this to, in an automated fashion, obtain a list of “structure types” for perovskites classified by which modes are active, then the precise structure is specified by the list of mode amplitudes. Other dimensional reduction techniques such as principle component analysis can potentially further reduce the dimension of each of these subspaces, and combined with clustering techniques automatically provide another level of “structure type” classification based not just on which modes are present, but also mode amplitudes. The automation of these techniques is a crucial feature as they can then be applied not just to perovskites as in the example, but scaled up to map out structure relations between all structures in databases such as the materials project or ICSD. In addition, automation of other group theory based analysis can be used. Not only the mode content, but also the symmetry allowed mode couplings, can be found automatically using pysotropy. Then databases of crystal structures can be used to identify materials likely to have strong couplings between modes. For example by checking if one mode is the primary order parameter, but some coupled modes have larger amplitudes than other materials of the same structure type. If one of these coupled modes is polar this process can be used as a strategy to find materials where electric fields can control characteristics typically not coupled to electric fields.

The study of functional materials has been greatly accelerated by developments in first principles methods to compute materials properties, models to capture the essential physics of a process, and tools which enable this process to be performed in a high throughput fashion where large datasets can yield new insights. Continued developments in these techniques enable both improved understanding of fundamental physics involved as well as facilitating

the discovery of new interesting and useful materials.

References

- [1] David Vanderbilt. *Berry Phases in Electronic Structure Theory: Electric Polarization, Orbital Magnetization and Topological Insulators*. Cambridge University Press, 2018.
- [2] Lauri Himanen, Amber Geurts, Adam Stuart Foster, and Patrick Rinke. Data-driven materials science: Status, challenges, and perspectives. *Advanced Science*, 6(21):1900808, 2019.
- [3] John Bonini David Vanderbilt and Karin M. Rabe. Berry flux diagonalization application to electric polarization, 2020.
- [4] J. Bonini, J. W. Bennett, P. Chandra, and K. M. Rabe. First-principles bulk-layer model for dielectric and piezoelectric responses in superlattices. *Physical Review B*, 99(10), Mar 2019.
- [5] R. O. Jones. Density functional theory: Its origins, rise to prominence, and future. *Reviews of Modern Physics*, 87(3):897–923, 2015.
- [6] Axel D. Becke. Perspective: Fifty years of density-functional theory in chemical physics. *The Journal of Chemical Physics*, 140(18):18A301, 2014.
- [7] P. Hohenberg and W. Kohn. Inhomogeneous electron gas. *Phys. Rev.*, 136:B864–B871, Nov 1964.
- [8] W. Kohn and L. J. Sham. Self-consistent equations including exchange and correlation effects. *Phys. Rev.*, 140:A1133–A1138, Nov 1965.
- [9] M. C. Payne, M. P. Teter, D. C. Allan, T. A. Arias, and J. D. Joannopoulos. Iterative minimization techniques for ab initio total-energy calculations: molecular dynamics and conjugate gradients. *Rev. Mod. Phys.*, 64:1045–1097, Oct 1992.
- [10] Stefano Baroni, Stefano de Gironcoli, Andrea Dal Corso, and Paolo Giannozzi. Phonons and related crystal properties from density-functional perturbation theory. *Rev. Mod. Phys.*, 73:515–562, Jul 2001.
- [11] Hendrik J. Monkhorst and James D. Pack. Special points for brillouin-zone integrations. *Phys. Rev. B*, 13:5188–5192, Jun 1976.
- [12] D. R. Hamann, M. Schlüter, and C. Chiang. Norm-conserving pseudopotentials. *Phys. Rev. Lett.*, 43:1494–1497, Nov 1979.
- [13] David Vanderbilt. Soft self-consistent pseudopotentials in a generalized eigenvalue formalism. *Phys. Rev. B*, 41:7892–7895, Apr 1990.
- [14] G. Kresse and D. Joubert. From ultrasoft pseudopotentials to the projector augmented-wave method. *Phys. Rev. B*, 59.

- [15] M. E. Lines and A. M. Glass. Principles and applications of ferroelectrics and related materials. Feb 2001.
- [16] Raffaele Resta. Macroscopic polarization in crystalline dielectrics: the geometric phase approach. *Rev. Mod. Phys.*, 66:899–915, Jul 1994.
- [17] R. Resta. Theory of the electric polarization in crystals. *Ferroelectrics*, 136(1):51–55, 1992.
- [18] R. D. King-Smith and David Vanderbilt. Theory of polarization of crystalline solids. *Physical Review B*, 47(3):1651–1654, 1993.
- [19] Jürgen Hafner, Christopher Wolverton, and Gerbrand Ceder. Toward computational materials design: the impact of density functional theory on materials research. *MRS Bulletin*, 31(9):659–668, 2006.
- [20] Alberto Franceschetti and Alex Zunger. The inverse band-structure problem of finding an atomic configuration with given electronic properties. *Nature*, 402(6757):60–63, 1999.
- [21] Craig J. Fennie and Karin M. Rabe. Magnetic and electric phase control in epitaxial eutiO_3 from first principles. *Phys. Rev. Lett.*, 97:267602, Dec 2006.
- [22] Zhenbin Wang, Jungmin Ha, Yoon Hwa Kim, Won Bin Im, Joanna McKittrick, and Shyue Ping Ong. Mining unexplored chemistries for phosphors for high-color-quality white-light-emitting diodes. *Joule*, 2(5):914–926, 2018.
- [23] Craig J. Fennie. Ferroelectrically induced weak ferromagnetism by design. *Physical Review Letters*, 100(16):167203, 2008.
- [24] Stefano Curtarolo, Gus L. W. Hart, Marco Buongiorno Nardelli, Natalio Mingo, Stefano Sanvito, and Ohad Levy. The high-throughput highway to computational materials design. *Nature Materials*, 12(3):191–201, 2013.
- [25] Shyue Ping Ong, William Davidson Richards, Anubhav Jain, Geoffroy Hautier, Michael Kocher, Shreyas Cholia, Dan Gunter, Vincent L. Chevrier, Kristin A. Persson, and Gerbrand Ceder. Python materials genomics (pymatgen): A robust, open-source python library for materials analysis. *Computational Materials Science*, 68:314 – 319, 2013.
- [26] Giovanni Pizzi, Andrea Cepellotti, Riccardo Sabatini, Nicola Marzari, and Boris Kozinsky. Aiida: Automated interactive infrastructure and database for computational science. *Computational Materials Science*, 111(nil):218–230, 2016.
- [27] Giovanni Pizzi, Atsushi Togo, and Boris Kozinsky. Provenance, workflows, and crystallographic tools in materials science: Aiida, spglib, and seekpath. *MRS Bulletin*, 43(9):696–702, 2018.
- [28] Sebastiaan. P. Huber, Spyros Zoupanos, Martin Uhrin, Leopold Talirz, Leonid Kahle, Rico Häuselmann, Dominik Gresch, Tiziano Müller, Aliaksandr V. Yakutovich, Casper W. Andersen, Francisco F. Ramirez, Carl S. Adorf, Fernando Gargiulo, Snehal Kumbhar, Elsa Passaro, Conrad Johnston, Andrius Merkys, Andrea Cepellotti, Nicolas Mounet, Nicola Marzari, Boris Kozinsky, and Giovanni Pizzi. Aiida 1.0, a

- scalable computational infrastructure for automated reproducible workflows and data provenance. *CoRR*, 2020.
- [29] Stefano Curtarolo, Wahyu Setyawan, Gus L.W. Hart, Michal Jahnatek, Roman V. Chepulskii, Richard H. Taylor, Shidong Wang, Junkai Xue, Kesong Yang, Ohad Levy, Michael J. Mehl, Harold T. Stokes, Denis O. Demchenko, and Dane Morgan. Aflow: an automatic framework for high-throughput materials discovery. *Computational Materials Science*, 58(nil):218–226, 2012.
- [30] Guido Petretto, Xavier Gonze, Geoffroy Hautier, and Gian-Marco Rignanese. Convergence and pitfalls of density functional perturbation theory phonons calculations from a high-throughput perspective. *CoRR*, 2017.
- [31] Gene Dresselhaus Mildred S. Dresselhaus and Ado Jorio. *Group Theory Application to the Physics of Condensed Matter*. Springer, 2008.
- [32] Nicole A. Benedek and Craig J. Fennie. Hybrid improper ferroelectricity: a mechanism for controllable polarization-magnetization coupling. *Physical Review Letters*, 106(10):107204, 2011.
- [33] Atsushi Togo and Isao Tanaka. *SpgLib*: a software library for crystal symmetry search. *CoRR*, 2018.
- [34] Mois Iliá Aroyo, Juan Manuel Perez-Mato, Cesar Capillas, Eli Kroumova, Svetoslav Ivantchev, Gotzon Madariaga, Asen Kirov, and Hans Wondratschek. Bilbao crystallographic server: I. databases and crystallographic computing programs. *Zeitschrift für Kristallographie - Crystalline Materials*, 221(1), Jan 2006.
- [35] Mois I. Aroyo, Asen Kirov, Cesar Capillas, J. M. Perez-Mato, and Hans Wondratschek. Bilbao crystallographic server. ii. representations of crystallographic point groups and space groups. *Acta Crystallographica Section A Foundations of Crystallography*, 62(2):115–128, Mar 2006.
- [36] D. M. Hatch H. T. Stokes and B. J. Campbell. Isotropy software suite. iso.byu.edu.
- [37] Karin M. Rabe. *Antiferroelectricity in Oxides: A Reexamination*, chapter 7, pages 221–244. John Wiley and Sons, Ltd.
- [38] Na Sai, B. Meyer, and David Vanderbilt. Compositional inversion symmetry breaking in ferroelectric perovskites. *Phys. Rev. Lett.*, 84:5636–5639, Jun 2000.
- [39] Nicola A. Spaldin. A beginner’s guide to the modern theory of polarization. *Journal of Solid State Chemistry*, 195(nil):2–10, 2012.
- [40] Takahiro Fukui, Yasuhiro Hatsugai, and Hiroshi Suzuki. Chern numbers in discretized brillouin zone: Efficient method of computing (spin) hall conductances. *Journal of the Physical Society of Japan*, 74(6):1674–1677, 2005.
- [41] D. R. Hamann. Optimized norm-conserving vanderbilt pseudopotentials. *Phys. Rev. B*, 88:085117, Aug 2013.

- [42] Xavier Gonze, Bernard Amadon, Gabriel Antonius, Frédéric Arnardi, Lucas Baguet, Jean-Michel Beuken, Jordan Bieder, François Bottin, Johann Bouchet, Eric Bousquet, Nils Brouwer, Fabien Bruneval, Guillaume Brunin, Théo Cavignac, Jean-Baptiste Charraud, Wei Chen, Michel Côté, Stefaan Cottenier, Jules Denier, Grégory Geneste, Philippe Ghosez, Matteo Giantomassi, Yannick Gillet, Olivier Gingras, Donald R. Hamann, Geoffroy Hautier, Xu He, Nicole Helbig, Natalie Holzwarth, Yongchao Jia, François Jollet, William Lafargue-Dit-Hauret, Kurt Lejaeghere, Miguel A.L. Marques, Alexandre Martin, Cyril Martins, Henrique P.C. Miranda, Francesco Naccarato, Kristin Persson, Guido Petretto, Valentin Planes, Yann Pouillon, Sergei Prokhorenko, Fabio Ricci, Gian-Marco Rignanese, Aldo H. Romero, Michael Marcus Schmitt, Marc Torrent, Michiel J. van Setten, Benoit Van Troeye, Matthieu J. Verstraete, Gilles Zerah, and Josef W. Zwanziger. The abinitproject: Impact, environment and recent developments. *Computer Physics Communications*, page 107042, 2019.
- [43] Yubo Zhang, Jianwei Sun, John P. Perdew, and Xifan Wu. Comparative first-principles studies of prototypical ferroelectric materials by lda, gga, and scan meta-gga. *Phys. Rev. B*, 96:035143, Jul 2017.
- [44] Darrell G. Schlom, Long-Qing Chen, Chang-Beom Eom, Karin M Rabe, Stephen K Streiffer, and Jean-Marc Triscone. Strain tuning of ferroelectric thin films. *Annual Review of Materials Research*, 37(1):589–626, Aug 2007.
- [45] Javier Junquera and Philippe Ghosez. First-principles study of ferroelectric oxide epitaxial thin films and superlattices: Role of the mechanical and electrical boundary conditions. *Journal of Computational and Theoretical Nanoscience*, 5(11):2071–2088, Nov 2008.
- [46] Matthew Dawber and Eric Bousquet. New developments in artificially layered ferroelectric oxide superlattices. *MRS Bulletin*, 38(12):1048–1055, 2013.
- [47] Fang Yang, Yan Liang, Li-Xia Liu, Qing Zhu, Wei-Hua Wang, Xue-Tao Zhu, and Jian-Dong Guo. Controlled growth of complex polar oxide films with atomically precise molecular beam epitaxy. *Frontiers of Physics*, 13(5):136802, Apr 2018.
- [48] Valentino R. Cooper and Karin M. Rabe. Enhancing piezoelectricity through polarization-strain coupling in ferroelectric superlattices. *Physical Review B*, 79(18):180101, May 2009.
- [49] J. B. Neaton and K. M. Rabe. Theory of polarization enhancement in epitaxial batio₃/sratio₃ superlattices. *Applied Physics Letters*, 82(10):1586–1588, Mar 2003.
- [50] W. Tian, J. C. Jiang, X. Q. Pan, J. H. Haeni, Y. L. Li, L. Q. Chen, D. G. Schlom, J. B. Neaton, K. M. Rabe, and Q. X. Jia. Structural evidence for enhanced polarization in a commensurate short-period batio₃ sratio₃ superlattice. *Applied Physics Letters*, 89(9):092905, Aug 2006.
- [51] F. A. Urtiev, V. G. Kukhar, and N. A. Pertsev. Phase diagrams of single-domain ferroelectric-dielectric superlattices. *Applied Physics Letters*, 90(25):252910, Jun 2007.
- [52] N. A. Pertsev, P.-E. Janolin, J.-M. Kiat, and Y. Uesu. Enhancing permittivity of ferroelectric superlattices via composition tuning. *Phys. Rev. B*, 81:144118, Apr 2010.

- [53] N. A. Pertsev, A. G. Zembilgotov, and A. K. Tagantsev. Effect of mechanical boundary conditions on phase diagrams of epitaxial ferroelectric thin films. *Phys. Rev. Lett.*, 80:1988–1991, Mar 1998.
- [54] Oswaldo Diéguez, Karin M. Rabe, and David Vanderbilt. First-principles study of epitaxial strain in perovskites. *Phys. Rev. B*, 72:144101, Oct 2005.
- [55] Ivo Souza, Jorge Íñiguez, and David Vanderbilt. First-principles approach to insulators in finite electric fields. *Phys. Rev. Lett.*, 89:117602, Aug 2002.
- [56] Massimiliano Stengel, Nicola A. Spaldin, and David Vanderbilt. Electric displacement as the fundamental variable in electronic-structure calculations. *Nature Physics*, 5(4):304–308, Feb 2009.
- [57] Karen Johnston, Xiangyang Huang, J. B. Neaton, and Karin M. Rabe. First-principles study of symmetry lowering and polarization in $\text{BaTiO}_3\text{SrTiO}_3$ superlattices with in-plane expansion. *Phys. Rev. B*, 71:100103, Mar 2005.
- [58] A. Q. Jiang, J. F. Scott, Huibin Lu, and Zhenghao Chen. Phase transitions and polarizations in epitaxial $\text{BaTiO}_3/\text{SrTiO}_3$ superlattices studied by second-harmonic generation. *Journal of Applied Physics*, 93(2):1180–1185, Jan 2003.
- [59] M. Dawber, C. Lichtensteiger, M. Cantoni, M. Veithen, P. Ghosez, K. Johnston, K. M. Rabe, and J.-M. Triscone. Unusual behavior of the ferroelectric polarization in $\text{PbTiO}_3/\text{SrTiO}_3$ superlattices. *Physical Review Letters*, 95(17):177601, Oct 2005.
- [60] Claudio Cazorla and Massimiliano Stengel. Ab initio design of charge-mismatched ferroelectric superlattices. *Physical Review B*, 90(2):020101, 2014.
- [61] Yurong Yang, Massimiliano Stengel, Wei Ren, X. H. Yan, and L. Bellaiche. Epitaxial short-period $\text{PbTiO}_3/\text{BiFeO}_3$ superlattices studied by first-principles calculations. *Physical Review B*, 86(14):144114, 2012.
- [62] Massimiliano Stengel, David Vanderbilt, and Nicola A. Spaldin. First-principles modeling of ferroelectric capacitors via constrained displacement field calculations. *Physical Review B*, 80(22):224110, Dec 2009.
- [63] X. Gonze, B. Amadon, P.-M. Anglade, J.-M. Beuken, F. Bottin, P. Boulanger, F. Bruneval, D. Caliste, R. Caracas, M. Côté, T. Deutsch, L. Genovese, Ph. Ghosez, M. Giantomassi, S. Goedecker, D.R. Hamann, P. Hermet, F. Jollet, G. Jomard, S. Leroux, M. Mancini, S. Mazevet, M.J.T. Oliveira, G. Onida, Y. Pouillon, T. Rangel, G.-M. Rignanese, D. Sangalli, R. Shaltaf, M. Torrent, M.J. Verstraete, G. Zerah, and J.W. Zwanziger. Abinit: First-principles approach to material and nanosystem properties. *Computer Physics Communications*, 180(12):2582 – 2615, 2009.
- [64] X Gonze, G Rignanese, M Verstraete, J Beuken, Y Pouillon, R Caracas, F Jollet, M Torrent, G Zerah, M Mikami, P Ghosez, M Veithen, J-Y Raty, V Olevano, F Bruneval, L Reining, R Godby, G Onida, D Hamann, and D Allan. A brief introduction to the abinit software package. *Zeitschrift für Kristallographie.*, 220(5/6):558–562, 2005.

- [65] X. Gonze, J.-M. Beuken, R. Caracas, F. Detraux, M. Fuchs, G.-M. Rignanese, L. Sindic, M. Verstraete, G. Zerah, F. Jollet, M. Torrent, A. Roy, M. Mikami, Ph. Ghosez, J.-Y. Raty, and D.C. Allan. First-principles computation of material properties: the {ABINIT} software project. *Computational Materials Science*, 25(3):478 – 492, 2002.
- [66] Joseph W. Bennett. Discovery and design of functional materials: Integration of database searching and first principles calculations. *Physics Procedia*, 34:14–23, 2012.
- [67] Jing Yang. Opium - pseudopotential generation project. <http://opium.sourceforge.net/>, 2018.
- [68] Xavier Gonze. First-principles responses of solids to atomic displacements and homogeneous electric fields: Implementation of a conjugate-gradient algorithm. *Phys. Rev. B*, 55:10337–10354, Apr 1997.
- [69] Xavier Gonze and Changyol Lee. Dynamical matrices, born effective charges, dielectric permittivity tensors, and interatomic force constants from density-functional perturbation theory. *Phys. Rev. B*, 55:10355–10368, Apr 1997.
- [70] Xifan Wu, David Vanderbilt, and D. R. Hamann. Systematic treatment of displacements, strains, and electric fields in density-functional perturbation theory. *Physical Review B*, 72(3):035105, Jul 2005.
- [71] Jiawang Hong and David Vanderbilt. Mapping the energy surface of pbti₃in multidimensional electric-displacement space. *Physical Review B*, 84(11):115107, Sep 2011.
- [72] Armin Antons, J. B. Neaton, Karin M. Rabe, and David Vanderbilt. Tunability of the dielectric response of epitaxially strained sr₂ti₃o₇ from first principles. *Physical Review B*, 71(2):024102, Jan 2005.
- [73] K. A. Müller and H. Burkard. Sr₂Ti₃O₇: An intrinsic quantum paraelectric below 4 k. *Phys. Rev. B*, 19:3593–3602, Apr 1979.
- [74] Oswaldo Diéguez, Silvia Tinte, A. Antons, Claudia Bungaro, J. B. Neaton, Karin M. Rabe, and David Vanderbilt. Ab initio study of the phase diagram of epitaxial bati₃o₇. *Phys. Rev. B*, 69:212101, Jun 2004.
- [75] Silvia Tinte, Karin M. Rabe, and David Vanderbilt. Anomalous enhancement of tetragonality in pbti₃ induced by negative pressure. *Physical Review B*, 68(14):144105, 2003.
- [76] I. Ponomareva, L. Bellaïche, and R. Resta. Dielectric anomalies in ferroelectric nanostructures. *Phys. Rev. Lett.*, 99:227601, Nov 2007.
- [77] Eric Bousquet, Matthew Dawber, Nicolas Stucki, Céline Lichtensteiger, Patrick Hermet, Stefano Gariglio, Jean-Marc Triscone, and Philippe Ghosez. Improper ferroelectricity in perovskite oxide artificial superlattices. *Nature*, 452(7188):732–736, 2008.
- [78] Pablo Aguado-Puente and Javier Junquera. Structural and energetic properties of domains in pbti₃/sr₂ti₃o₇ superlattices from first principles. *Phys. Rev. B*, 85:184105, May 2012.
- [79] Yuanjun Zhou and Karin M. Rabe. Determination of ground-state and low-energy structures of perovskite superlattices from first principles. *Phys. Rev. B*, 89:214108, Jun 2014.

- [80] James M. Rondinelli and Nicola A. Spaldin. Substrate coherency driven octahedral rotations in perovskite oxide films. *Phys. Rev. B*, 82:113402, Sep 2010.
- [81] Takuro Ikeda. *Fundamentals of piezoelectricity*. Oxford University Press, 1 1997.
- [82] Xinjie Wang and David Vanderbilt. First-principles perturbative computation of dielectric and born charge tensors in finite electric fields. *Physical Review B*, 75(11):115116, Mar 2007.
- [83] Dorian M. Hatch Harold T. Stokes. Coupled order parameters in the landau theory of phase transitions in solids. *Phase Transitions*, 34:53–67, 1991.
- [84] Sean Kerman, Branton J. Campbell, Kiran K. Satyavarapu, Harold T. Stokes, Francesca Perselli, and John S. O. Evans. The superstructure determination of displacive distortions via symmetry-mode analysis. *Acta Crystallographica Section A Foundations of Crystallography*, 68(2):222–234, 2012.
- [85] Harold T. Stokes and Dorian M. Hatch. Findsym: Program for identifying the space-group symmetry of a crystal. *Journal of Applied Crystallography*, 38(1):237–238, 2005.
- [86] Harold T. Stokes. Using symmetry in frozen phonon calculations. *Ferroelectrics*, 164:183–188, 1995.
- [87] Dorian M. Hatch and Harold T. Stokes. Invariants: program for obtaining a list of invariant polynomials of the order-parameter components associated with irreducible representations of a space group. *Journal of Applied Crystallography*, 36:951–592, 2003.
- [88] Michael W. Lufaso and Patrick M. Woodward. Prediction of the crystal structures of perovskites using the software program spuds. *Acta Crystallographica Section B Structural Science*, 57(6):725–738, Nov 2001.
- [89] Dorian M. Hatch and Harold T. Stokes. Complete listing of order parameters for a crystalline phase transition: a solution to the generalized inverse landau problem. *Physical Review B*, 65(1):014113, 2001.